The influence of subseismic-scale fracture interconnectivity on fluid flow in fracture corridors of the Brejões carbonate karst system, Brazil

Furtado, Carla P.Q.; Medeiros, Walter E.; Borges, Sergio V.; Lopes, Juliana A.G.; Bezerra, Francisco H.R.; Lima-Filho, Francisco P.; Maia, Rubson P.; Bertotti, Giovanni; Auler, Augusto S.; Teixeira, Washington L.E.

DOI
10.1016/j.marpetgeo.2022.105689

Publication date
2022

Document Version
Final published version

Published in
Marine and Petroleum Geology

Citation (APA)
Furtado, C. P. Q., Medeiros, W. E., Borges, S. V., Lopes, J. A. G., Bezerra, F. H. R., Lima-Filho, F. P., Maia, R. P., Bertotti, G., Auler, A. S., & Teixeira, W. L. E. (2022). The influence of subseismic-scale fracture interconnectivity on fluid flow in fracture corridors of the Brejões carbonate karst system, Brazil. *Marine and Petroleum Geology*, *141*, 1-21. Article 105689. https://doi.org/10.1016/j.marpetgeo.2022.105689

Marine and Petroleum Geology 141 (2022) 105689

Contents lists available at ScienceDirect

Marine and Petroleum Geology

journal homepage: www.elsevier.com/locate/marpetgeo

The influence of subseismic-scale fracture interconnectivity on fluid flow in fracture corridors of the Brejões carbonate karst system, Brazil

Carla P.Q. Furtado [a], Walter E. Medeiros [a,b,c,*], Sergio V. Borges [d], Juliana A.G. Lopes [a], Francisco H.R. Bezerra [a,e], Francisco P. Lima-Filho [a,e], Rubson P. Maia [f], Giovanni Bertotti [g], Augusto S. Auler [h], Washington L.E. Teixeira [a]

[a] Post-Graduation Program on Geodynamics and Geophysics, Federal University of Rio Grande do Norte, Natal, Brazil
[b] Department of Geophysics, Federal University of Rio Grande do Norte, Natal, Brazil
[c] INCT-GP/CNPq/CAPES-National Institute of Science and Technology in Petroleum Geophysics, Brazil
[d] Federal Institute of Education, Science and Technology of Rio Grande do Norte - IFRN, Natal, Brazil
[e] Department of Geology, Federal University of Rio Grande do Norte, Natal, Brazil
[f] Department of Geography, Federal University of Ceará, Fortaleza, Brazil
[g] Faculty of Civil Engineering and Geosciences, Delft University of Technology, Stevinweg 1, 2628, CN, Delft, the Netherlands
[h] Instituto do Carste, Carste Ciência e Meio Ambiente, Belo Horizonte, Brazil

ARTICLE INFO

Keywords:
Carbonate rocks
Carbonate reservoirs
Karst
Fracture corridors
Caves

ABSTRACT

The present study used a multitool approach to characterize fractures of several orders of magnitude in large fracture corridors, caves, and canyons to investigate their impact on fluid flow in carbonate units. The study area is the Brejões carbonate karst system that is located in the Neoproterozoic Salitre Formation in the Irecê Basin, São Francisco Craton, Brazil. The approach included satellite imagery, used for interpreting the regional structural context, Unmanned Aerial Vehicle (UAV) and ground-based Light Detection And Ranging (LiDAR) imagery, used for detailed structural interpretation. Regional interpretation revealed that fracture corridors, caves and canyons occur along a N–S-oriented anticline hinge. An advanced stage of karstification caused fracture enlargement and intrabed dissolution, and the formation of caves and canyons. A river captured by the highly fractured zone along the anticline hinge played an important role as an erosive agent. Detailed characterization of fracture corridors comprised structural analysis, topological studies, persistence estimations, power-law fitting of fracture trace length distributions, and identification of network backbones. Our results indicate that fracture corridors comprise four subvertical fracture sets: N–S and E-W and a conjugate pair, NNE-SSW and NW-SE. Fractures observed in the caves show the same dominant directions. Fracture directions are consistent with a common origin associated with the anticline folding. Fracture traces range from 1.0 m to 300 m, comprising both subseismic (<50 m) and seismic scale fractures (>50 m). Networks have dominance of node terminations Y and X (notably Y), C_B values higher than 1.8, high P_{20} and P_{21} persistence values, and highly interconnected backbones. Fracture network connectivity is associated with power-law exponents greater than 2.5 for the fracture trace distributions, indicating large influence of subseismic-scale fractures on fluid flow. As the final result of folding and karstification, large volumes of secondary macroporosity were created, particularly in the zone of maximum fracture intensity around the hinge zone of the anticline. This scenario can be used to understand better oil reservoirs formed in similar structural controls in near-surface conditions.

1. Introduction

Predicting how subseismic-scale fractures and karst features influence oil reservoirs has become a challenge to the industry. Understanding the development and distribution of these features is fundamental to reducing uncertainties related to reservoir characterization

* Corresponding author. Post-Graduation Program on Geodynamics and Geophysics, Federal University of Rio Grande do Norte, Natal, Brazil.
E-mail addresses: cpqfurtado@hotmail.com (C.P.Q. Furtado), walter@geofisica.ufrn.br (W.E. Medeiros), sergiovieiraborges@gmail.com (S.V. Borges), juliana.aglopes@yahoo.com.br (J.A.G. Lopes), hilario.bezerra@ufrn.br (F.H.R. Bezerra), pinheiro.lima@ufrn.br (F.P. Lima-Filho), rubsonmaia7@gmail.com (R.P. Maia), G.Bertotti@tudelft.nl (G. Bertotti), aauler@gmail.com (A.S. Auler), wasluiz@gmail.com (W.L.E. Teixeira).

https://doi.org/10.1016/j.marpetgeo.2022.105689
Received 19 January 2022; Received in revised form 10 April 2022; Accepted 11 April 2022
Available online 16 April 2022

and field performance (Gillespie et al., 2011). Previous studies on outcropping analogs of oil reservoirs revealed the key role of fractures in the subsurface fluid-flow pattern (Ogata et al., 2014). In low-permeability matrix rocks, such as carbonates, open fractures often act as preferential conduits, composing the main pathways for fluid flow and increasing the storage capacity (Agosta et al., 2010; Boersma et al., 2019). On the other hand, closed fractures can act as seals, permeability barriers or baffles that inhibit fluid flow (Larsen et al., 2010).

The pre-existing porosity/permeability associated with fracture networks can commonly be enhanced by karst processes (e.g., Lopes et al., 2022) through dissolution and mechanical erosion, improving the flow and storage potential of fractured reservoirs (Trice, 2005). In particular, fracture corridors formed by karstified fracture networks can also be included as key components of reservoirs. Fracture corridors compose high-permeability zones, and are commonly developed along multiple fracture sets with different orientations (Questiaux et al., 2010). In addition, they might contribute to disrupting top-seal integrity and can play a role in seal-bypass systems interconnecting reservoirs at different stratigraphic levels (Questiaux et al., 2010; Ogata et al., 2014).

The insufficient sampling of nonmatrix features in subsurface measurements might lead to the underestimation of the role of fracture corridors, notably of their subseismic-scale components (Loucks, 2001; Medekenova and Jones, 2014). Multiscale statistical fracture analyses can provide parameters to improve fracture network representation in models to understand better the dissolution process in fracture corridors (Questiaux et al., 2010; Agosta et al., 2010; Gillespie et al., 2011; Panza et al., 2016) and allow fluid flow modeling to assist reservoir development (Gholipour et al., 2016).

Recent studies have demonstrated that representing the geometric and spatial parameters of fracture networks is as important as evaluating their connectivity through topological parameters (Sanderson and Nixon, 2015, 2018; Thiele et al., 2016; Dimmen et al., 2017; Primaleon et al., 2020). In this way, parameters estimated from the node type and branch classifications provide network descriptions and can evaluate structural complexities. Statistical structural analyses performed in outcrop analogs cannot be directly applied to deep subsurface predictions (Gillespie et al., 2011) due to differences in stratigraphy, facies, uplift history, and associated stress release, as pointed out by Panza et al. (2016). However, studying outcropping scenarios might help us understand what can occur in subsurface conditions. These studies allow detailed structural characterization of fracture networks covering several orders of magnitude, thus offering better conditions to mitigate censoring and truncation effects (Sanderson and Nixon, 2015). As a result, a better understanding of how secondary porosity and permeability originate is gained to make better predictions (Primaleon et al., 2020).

A way to obtain more information about fractures and karst features on analogs is to perform structural analyses using tridimensional imaging (e.g., Bourdon et al., 2004; Gillespie et al., 2011). In particular, remote sensing by satellite images, Unmanned Aerial Vehicle (UAV) imagery, and Light Detection And Ranging (LiDAR) datasets provide material to characterize structures of several orders of magnitude in expositions of fracture corridors, caves and canyons. LiDAR technology has also proven to be a valuable tool in geological mapping studies (Buckley et al., 2008; Drews et al., 2018), elaboration of digital elevation models (DEMs) (Slob et al., 2002), and virtual outcrop models of hydrocarbon reservoir analogs (Bellian et al., 2005; Enge et al., 2007; Fabuel-Perez et al., 2010; Marques et al., 2020). In 3D cave mappings, ground-based LiDAR data promote a change of perspective in geomorphological studies by allowing the analysis of the morphology and volume of the voids and conduits (Silvestre et al., 2015; Gallay et al., 2016; De Waele et al., 2018) and the analysis of structural and hydrogeological characteristics of the cave bedrock (Buchroithner and Gaisecker, 2009).

We present a detailed study of a near-surface carbonate karst system, where fracture corridors, caves and canyons were jointly formed along an anticline hinge. The formation of fracture corridors conditioned by folding is a well-known process (e.g., Jadoon et al., 2006; Singh et al., 2008; Questiaux et al., 2010; Ogata et al., 2014; Souque et al., 2019). Our aim is to use this well-known structural conditioning to support a detailed quantitative characterization of fracture corridors, to go beyond qualitative descriptions, to evidence the importance of subseismic fractures in the connectivity of fracture corridors. To this end, we use a multi-method approach, combining classic structural studies, fracture trace length analyses (including adherence to a power law and backbone isolation), persistence estimations, and topological characterization.

2. Geological and speleological settings

2.1. Tectonic evolution

The study area is part of the Irecê Basin, a Neoproterozoic (900-600 Ma) cratonic basin (Souza et al., 1993) located in the central-northern region of the São Francisco Craton (SFC), northeastern Brazil (Fig. 1). During the Brasiliano Orogeny (740-560 Ma), the Irecê Basin experienced at least two compressional events, which affected the northern edge of the SFC in the Brasiliano collisions (Lagoeiro, 1990; Caxito and Uhlein, 2013; Brito Neves et al., 2014). As a result, the mobile belts of the province overthrust the SFC; for example, the edge of the nappes of the Riacho do Pontal mobile belt are located approximately 50 km to the south from the contact between the SFC and Borborema Province crustal blocks (Oliveira and Medeiros, 2018).

The main deformation structures recorded in the Irecê Basin due to the first compressional event included southward tectonic vergence, generating an E-W system of reverse faults, where gentle to open reverse drag folds with southward vergence associated with slips along beddings occurred. A secondary and younger deformation structure was related to E-W-oriented horizontal compression, which resulted in fewer expressive folds and faults than those in the previous event, but was no less important since it contributes to the present control of rivers and relief (Kuchenbecker et al., 2011; Borges et al., 2016).

2.2. Geological units

The sedimentary rocks in the Irecê Basin belong to the Una Group (Fig. 1c), which forms an extensive carbonate platform that is more than 300,000 km^2 in area (Misi and Veizer, 1998). The basement of the basin is composed of Paleoproterozoic to Mesoproterozoic siliciclastic metasedimentary rocks and Archaean metamorphic units (Misi et al., 2011). The sedimentary rocks in the Una Group form an erosive and angular unconformity over the basement rocks (Kuchenbecker et al., 2011; Guimaraes et al., 2011; Brito Neves et al., 2014). The sedimentary rocks of the Una Group include diamictites, sandstones, and pelites from the Bebedouro Formation and carbonate rocks from the Salitre Formation, the latter forming the framework of the study area (Fig. 1c).

The Salitre Formation overlies the Bebedouro Formation or the basement rocks (Misi and Veizer, 1998; Bizzi et al., 2003; Misi et al., 2011) and has an estimated maximum age of 669 ± 14 Ma (Santana et al., 2021). The Salitre Formation is composed of a succession of carbonate rocks, with thicknesses varying between 550 and 1000 m (Misi, 1993). There are also rare intercalations of pelites (Misi, 1979; Leão and Dominguez, 1992). The carbonate rocks were deposited in a shallow marine environment on a prevailing ramp-type platform (Santana et al., 2021) during at least two transgressive-regressive cycles (Dominguez, 1993; Misi and Veizer, 1998).

According to Misi and Silva (1996), the Salitre Formation comprises five informal units, from the bottom to the top (Fig. 1c): C, red argillaceous dolostones; B, laminated limestones; B1, siliceous dolomites, dolarenites (siliceous and politic), and dololutites; A, siltstones, calcitic clays, and marl; and A1, calcilutites and oolitic and pisolitic limestones. Boersma et al. (2019) included the Brejões outcrops and the Brejões I cave segment in units A1 (oolitic limestone) and B (laminated limestone), respectively. The carbonates composing the Brejões system

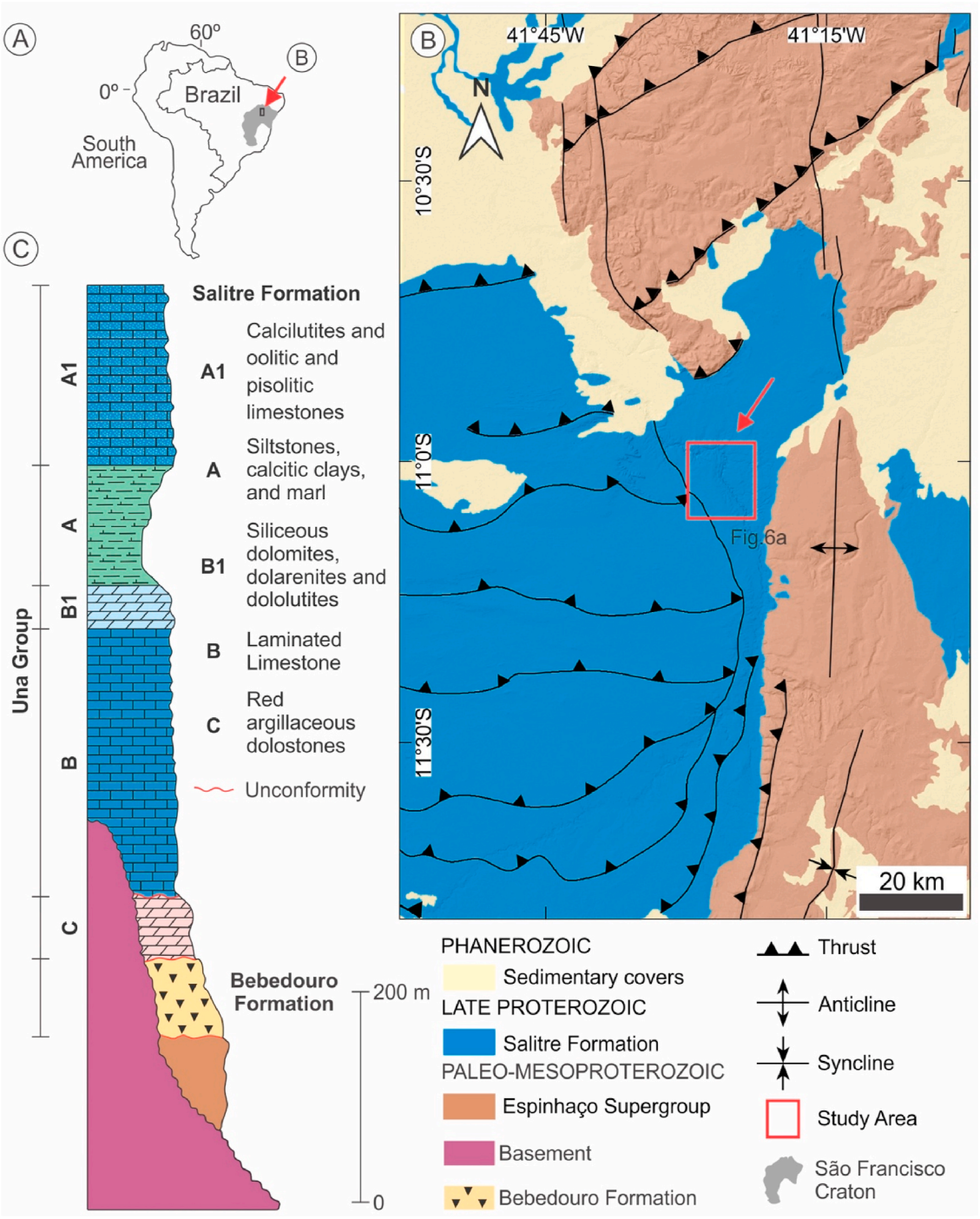

Fig. 1. Tectonic and stratigraphic setting of the study area: (A) The South American continent and location of the study area as part of the São Francisco Craton (modified from Bizzi et al., 2003). (B) Simplified geologic map of the northern part of the Irecê Basin (modified from Souza et al., 1993). The study area is represented by the red rectangle in (B) that corresponds to Fig. 5a. (C) Simplified stratigraphic column of the Una Group (modified from Santana et al., 2021). (For interpretation of the references to colour in this figure legend, the reader is referred to the Web version of this article.)

correspond to sub-horizontal limestone beds that are laterally continuous but have variable thickness; they present both stratabound and non-stratabound fractures. In the study area, laminated mudstones and gray to black grainstones are the most common carbonate rocks (Boersma et al., 2019).

2.3. Geomorphological setting

The study site (Fig. 2) is part of a vast karst area (Figs. 3 and 4) developed on the carbonate rocks of the Salitre Formation (Auler, 2019). The area has a semiarid climate and is crossed by the Jacaré River (Figs. 2 and 3a). This river flows from south to north and is one of the few perennial rivers in the region. Fluvial incision has developed a canyon over 100 m deep in some places, created mostly due to the collapse of ancient caves. However, caves are still preserved in a few places, and the canyon is interrupted as the river flows underground (Fig. 3b).

Brejões is the main cave system in the area and is divided into three segments, named Brejões I, II and III (Fig. 2). Its development is associated with the Jacaré River. The upstream segment Brejões I is the

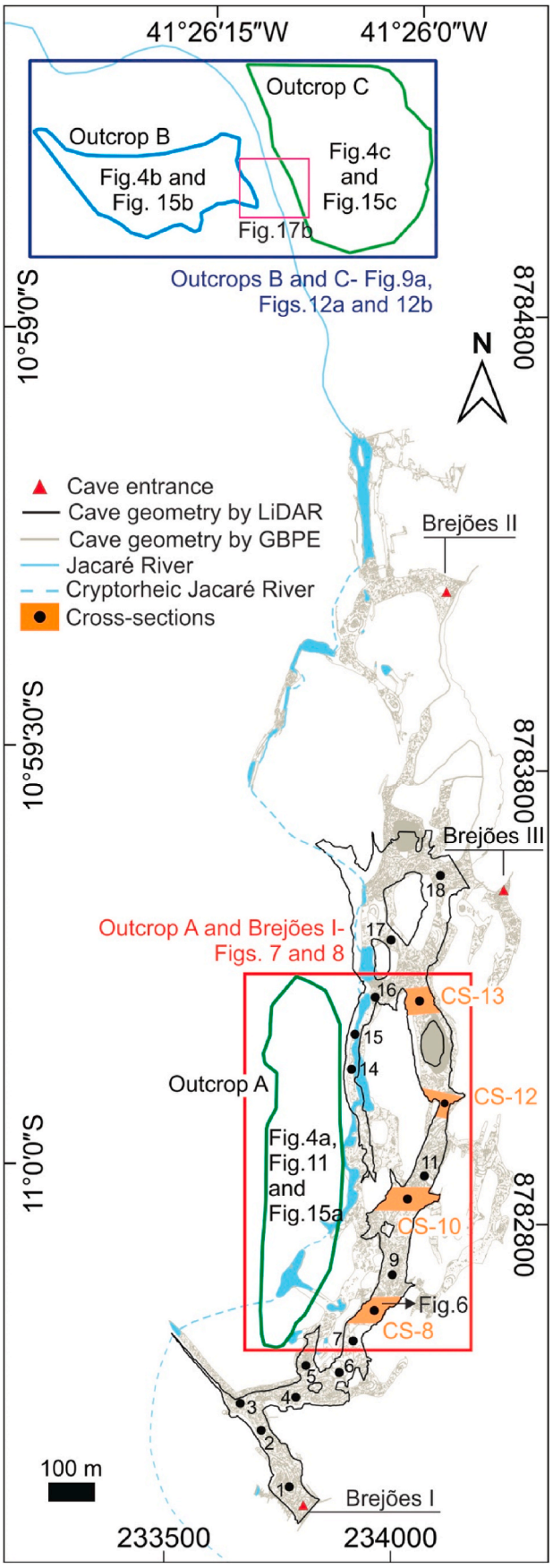

(caption on next column)

Fig. 2. General view of the study area locating all outcrops and caves. Outcrops A (dark green polygon), B (light blue polygon), and C (light green polygon) were used to perform the statistical characterization of the fracture networks. The dark blue rectangle encompasses outcrops B and C, which were also used to compare persistence variation along an anticline coinciding with the Jacaré river valley. The pink rectangle represents the area of the block diagram used to show the actual configuration of Brejões canyon (Fig. 17b). The red rectangle encompasses sectors of Outcrop A, and the contiguous subsurface caves (filled orange polygons), which is used to compare fracture networks in corridors and caves. The black dots show the cave cross-sections located along the Brejões I System. This figure is presented in geographic and UTM coordinate systems to facilitate localization at different scales. Cave mapping done by GBPE ("Grupo Bambuí de Pesquisas Espeleológicas") (https://bambuiespeleo.wordpress.com/). (For interpretation of the references to colour in this figure legend, the reader is referred to the Web version of this article.)

longest segment and is our main study site. Brejões II is the downstream segment and is connected by underground drainages with Brejões I. Finally, Brejões III is a short lateral passage not connected to the river (Rubbioli et al., 2019).

The Brejões I segment contains a series of approximately parallel passages trending S–N related to former and active routes of the underground Jacaré River. The passages can reach impressive dimensions (Fig. 3), being commonly over 40 m high and 50 m wide, with the main entrance passage being approximately 100 m high (Fig. 3b). The river currently occupies the western passages of the cave, which contain several slumped sections. Without an active drainage, the other cave passages are dry and contain floors covered by clastic deposits, including massive collapsed blocks. The caves exhibit a trend, from passages presenting high elevation above the river level in the eastern sector to passages near the river level in the western sector. Most passages show considerable modifications due to collapse processes, especially the largest ones. Due to the advanced stage of the collapse processes, sometimes it is difficult to identify the morphology of the original cave. In some areas, there are dome-shaped chambers, some of which reach the surface, resulting in openings (skylights) that bring light and surface runoff toward the caves (Fig. 3c, d and 3e).

Surface topography also shows imprints from the underground cave processes. For example, a dry canyon runs east from the cave passages (Fig. 3a and b), representing former hydrologically active caves of an earlier phase of Brejões I, which have now collapsed. These collapsed karstic valleys show abrupt limestone scarps and are surrounded by large, fractured pavements (Fig. 4), having a gentle dip toward the west (Boersma et al., 2019). The large carbonate outcrops expose fracture corridors (Fig. 4) with subvertical fractures generally enlarged by dissolution. Isolated truncated dolines might be aligned with existing passages, indicating that they resulted from the partial collapse of conduits (Fig. 3e).

Cave passages in the Brejões I segment are controlled by bedding planes and fractures (Berbert-Born and Karmann, 2000). Despite considerable modifications due to ceiling collapses, the straight orientation of some passages, such as entrance sections, indicates fracture control. In the younger active passages in the western sector, bedding control is indicated by flat ceilings and the general horizontal arrangement of the passages.

The carbonate sequences of the Salitre Formation often contain pyrite-rich layers, which can commonly be observed in outcrops inside the Brejões I segment. Exposure of pyrite to oxygenated groundwater releases sulfuric acid, a powerful booster of speleogenesis (Auler and Smart, 2003). In addition, the long geologic history of the Proterozoic carbonate sequences in the Una Group has made them natural targets for dissolution by the possible deep-seated ascending flow. This process has resulted in hypogene cave formation. This has been proposed to explain the giant maze caves in the same geological framework to the east (Klimchouk et al., 2016; Auler et al., 2017) and the southern portion of the Irecê Basin (Bertotti et al., 2020).

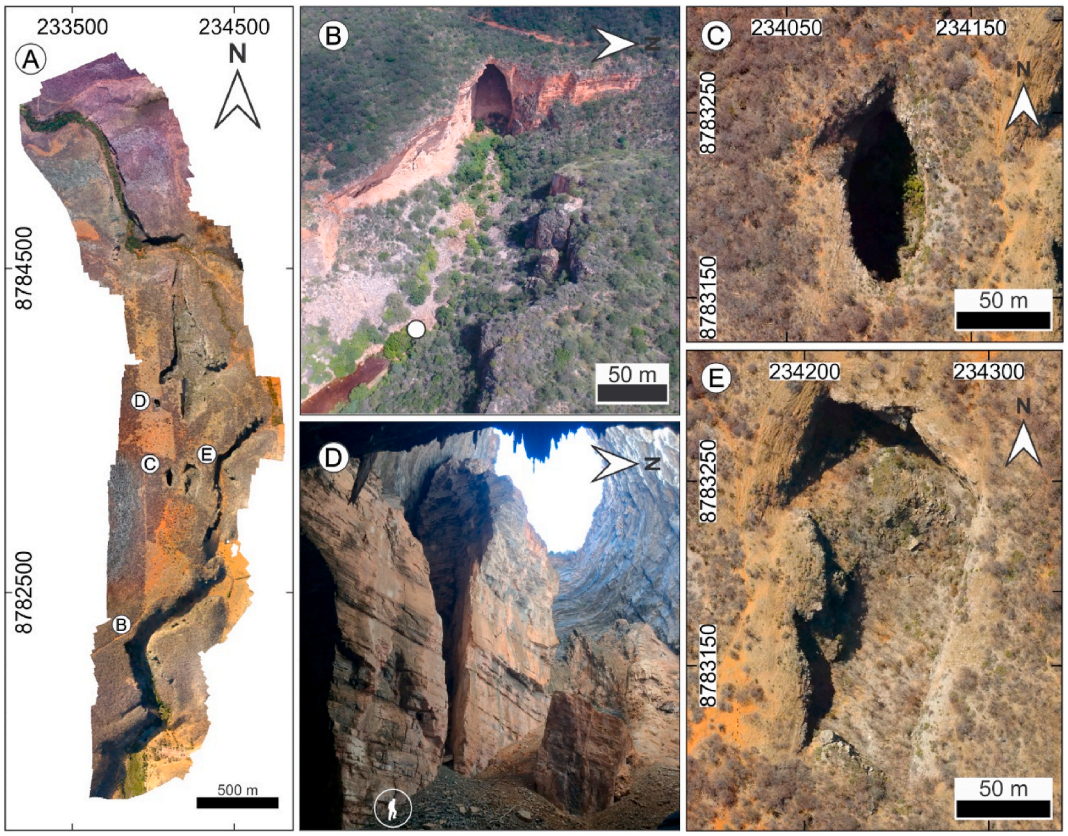

Fig. 3. Main geomorphological features in Brejões Cave System. A) UAV imagery of Brejões System, including the locations of Brejões I entrance and three dolines (one representing the collapsed portion of a conduit); Figure A corresponds to the area outlined in Fig. 2 as a dark green polygon. B) Aerial view of the main entrance passage (approximately 100 m high); the white dot indicates the point where the Jacaré river sinks underground. C) Detail of the first southern doline (skylight). D) Internal part of the cave that corresponds to the second northern doline (skylight); the scale notion is given in the bottom of the figure as a person drawn in white. E) Aerial view of an elongated doline related to a partially collapsed cave passage parallel to the first southern doline. (For interpretation of the references to colour in this figure legend, the reader is referred to the Web version of this article.)

Despite the possible importance of deep-seated hypogene and/or pyrite oxidation processes, the Brejões cave system developed mostly through classical epigenic speleogenesis, related to the fluvial incision of the Jacaré river. River downcutting is responsible for the general vertical stacking of cave passages and is still the main cave forming process in the active river passages in the western part of the cave (Berbert-Born and Karmann, 2000). Following the draining of the older upper passages, the collapse of the ceiling and walls progressively modified the passages, leading to a massive accumulation of fallen fragments on the floor and upward migration of the ceiling. Eventually, ceiling collapse led to the generation of skylights and the development of surface dolines and canyons.

3. Imagery tools

The primary material of this study comprises remote sensing by satellite images, UAV imagery, and ground-based LiDAR data. Satellite images were used to characterize the regional structural context of the study area, while UAV and LiDAR images were used for detailed structural characterization of the fracture corridors and caves, respectively.

3.1. Satellite imagery

Broad-scale satellite imagery analyses were carried out to obtain an overview of the geomorphological and structural features of the study area to identify the regional structural setting. We used a digital elevation model (DEM) by Alos Palsar with a 12.5 m resolution. Using QGIS software, a DEM was processed with the multidirection oblique (MDOW) Hillshade technique using an azimuth equal to 270°, elevation equal to 45°, and vertical exaggeration equal to 3, resulting in the images shown in Fig. 5.

3.2. UAV imagery

We used photogrammetric imaging to increase the mapping resolution to a decimeter scale. The aerial photogrammetric survey was performed with the UAV DJI Phantom 4 PRO model with a 21-megapixel camera. The data were obtained with 80% frontal and lateral overlap with a mean surface height of 80 m, totaling 998 photos. The covered area was 4300 m × 900 m. UAV image processing was performed in Agisoft Photoscan® software, resulting in an orthomosaic with 0.08 m of resolution that allowed the construction of the DEM. Typical resulting images are shown in Figs. 3 and 4.

3.3. LiDAR imagery

The study investigated the (3D) fracture network in the caves with Terrestrial Laser Scanning (TLS) equipment, VZ 1000 model, manufactured by RIEGL. Time of flight point acquisition was used by applying the "cloud-to-cloud" technique with 15% overlap. The precision and accuracy of the TLS positions and point clouds were guaranteed by using the *TOPCON CTS-3007 Total Station* and real-time kinematic (RTK-GNSS) acquisition technique. LiDAR data were processed with the software Riscan Pro following the steps defined by Buckley et al. (2008).

A total of 3500 m linear profiles of cave conduits were surveyed with precision limits of 1 cm (horizontal) and 3 cm (vertical). We used the

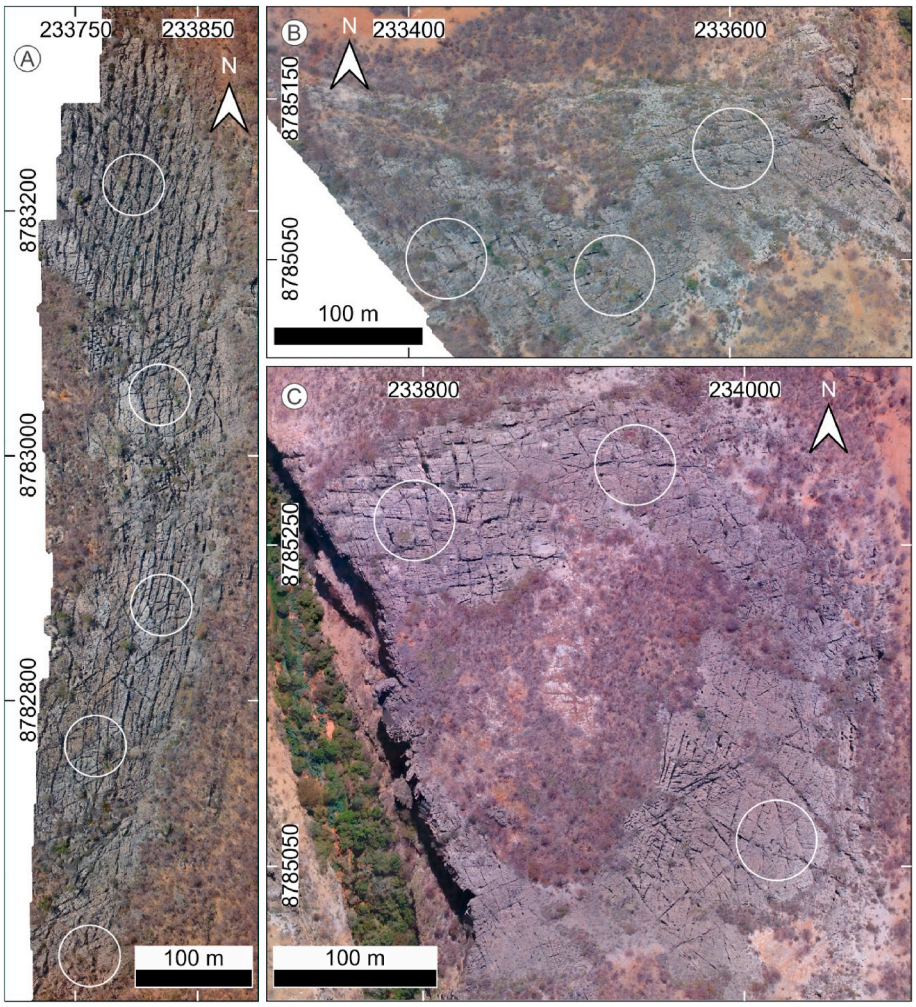

Fig. 4. Outcrops A (in A), B (in B), and C (in C) in the Brejões area. All images show that the outcrop pavements are densely fractured and karstified. White circles enclose the scan areas used for topological analyses (Fig. 16); each represents a scan over a circular area with a diameter equal to 50 m.

SIRGAS2000 geodetic georeferenced system projected on a UTM system (24S). LiDAR point cloud analyses were performed using CloudCompare software. Two additional steps were applied to the Brejões point cloud: Hough normal computation, which is a mathematical resource to improve the definition of angular forms, and eye-dome lighting, which is an image-based shading technique applied to improve depth perception (Girardeau-Montaut, 2015). Typical resulting images are shown in Figs. 6 and 7.

4. Structural analysis methodologies

The structural characterization of the study area was carried out in two main phases. In the first phase, based on the interpretation of satellite images, we characterized the regional structural context, when we interpret that the study area comprises an anticline hinge (see details in Section 5.2). The second characterization phase was carried out already knowing this context. In this second phase, detailed statistical characterization of fracture corridors and caves was done using UAV images and ground-based LiDAR images, respectively (see details in Sections 5.3-5.6). As we follow the classic order of presenting methodological aspects in advance, the methodologies used in the detailed interpretation are described below.

Three approaches were used to characterize the fracture networks in the study area: 1st) statistical characterization of entire fracture corridor outcrops, 2nd) statistical characterization of fractures exposed on cave surfaces, and 3rd) subsampling of fracture corridors with scan areas. The term fracture is used in this study to refer to any discontinuity, such as veins, stylolites, joints, or faults.

4.1. Statistical characterization of entire fracture corridors

This approach was used to characterize fracture trace statistics, persistence parameters, adherence of fracture trace length distributions to a power law, and backbone isolation. An auxiliary digital scanline was also done. Using UAV images, two-dimensional (2D) quantitative analyses of fractures were performed in the three outcrops shown in Fig. 2 and named Outcrop A (149,784 m^2), Outcrop B (117,600 m^2), and Outcrop C (171,282 m^2). As schematically shown in Fig. 2, Outcrop A is located on the slope above the Brejões I segment, while outcrops B and C are on the opposite banks of the Jacaré River in the northern portion of the Brejões II segment.

An interpretive partition of Outcrop A into four different structural domains (A-I, A-II, A-III and A-IV) was done based on differences in fracture direction statistics (Fig. 8; details are given in Section 5.3). This partition was used as a support to select adjacent sectors of the caves (Fig. 7) to carry out a comparative study of fracture parameters in corridors (based on UAV images) and caves (based on LiDAR images) (Fig. 8). The vertical distance from fracture corridors to caves varies from 63 m to 105 m, while the lateral distance on the surface varies between 121 m and 231 m (Fig. 7).

Similar structural partitions were not done in outcrops B and C. Therefore, in these outcrops, denominations B–I to B-III and C–I to C-III,

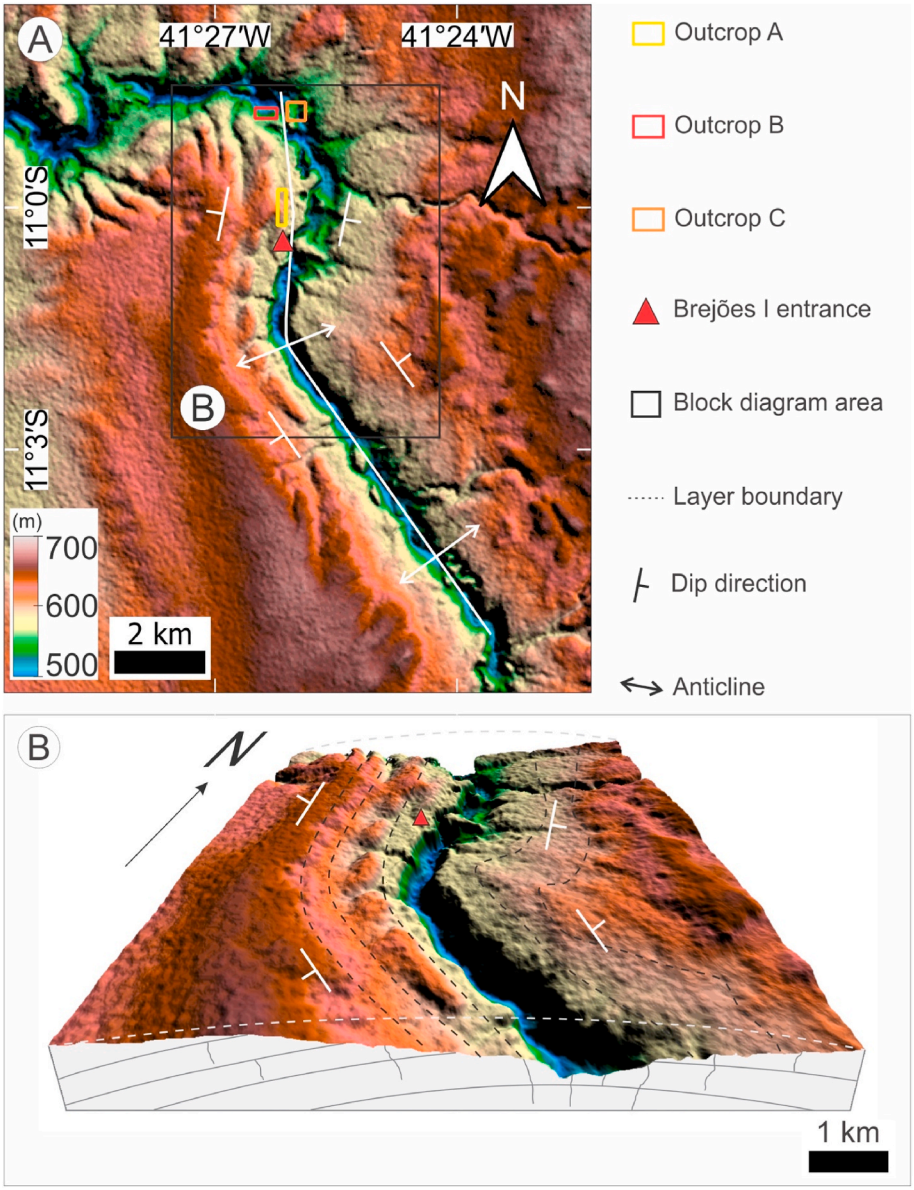

Fig. 5. Digital elevation model for the study area that was constructed from Alos Palsar satellite images. A) Plan view showing the spatial distribution of the outcrops around the interpreted fold hinge of an anticline, whose axis coincides with the river valley; outcrops A (yellow square) and B (red square) are located on the west fold limb, whilst Outcrop C (orange square) is on the east fold limb of the anticline; white arrows illustrate the dip direction of the layers. B) Block diagram shows that the layers have opposite dip directions related to the interpreted anticline hinge. (For interpretation of the references to colour in this figure legend, the reader is referred to the Web version of this article.)

respectively, as in Fig. 9, refer just to sectors of the outcrop where sampling scan areas for topological analyses were located.

4.1.1. Fracture trace characterization

Using the open-source software QGIS 3.12v, fractures were identified and digitized on all outcrops and traced as polylines from tip to tip while keeping their original geometry (Weismüller et al., 2020). As a result, each fracture is represented by a trace, from where spatial parameters, such as orientation, trace length, intensity and density, can be measured. Statistical analyses were performed with the open-source software FracPaQ, following Healy et al. (2017). Typical results are shown in Figs. 8a, 9 and 10.

4.1.2. Persistence estimations

We obtained maps of fracture persistence (Dershowitz and Herda, 1992). Specifically, we obtained fracture intensity P_{21} maps, which express the variation of total trace length per unit area (dimension $[L^{-1}]$), and fracture density P_{20} maps, which express the variation of the number of fractures (N_L) per unit area (dimension $[L^{-2}]$).

Persistence maps were automatically generated with FracPaQ software, according to Dershowitz and Herda (1992) and using the automatic scan procedure of Mauldon et al. (2001). Typical results are shown in Figs. 11 and 12. In particular, Fig. 12c shows the results of the digital scanline obtained according to Priest (1993).

Although persistence estimates are not directly related to connectivity, a high persistence value (either P_{20} or P_{21}) is a clue to a high degree of connectivity. In addition, persistence estimates are easily incorporated into models of macroscopic media equivalent to fractured media (Antonellini et al., 2014).

4.1.3. Power law and backbone isolation

Fracture network complexity was also assessed by analyzing the *probability* of occurrence of fracture trace lengths both on fracture corridors and caves. Several studies (e.g., Bonnet et al., 2001; Bertrand et al., 2015; Miranda et al., 2018; Giuffrida et al., 2019) have documented that the probability distribution $p(l)$ of the fracture trace length l in a chosen length interval $[l_{min}, l_{max}]$ might follow a power law given by:

$$p(l) = \beta\, l^{-\alpha} \quad (1)$$

where the trace length l represents the discrete interval $[l, l + \Delta l]$, β is a density parameter, and α is an exponent that commonly varies between

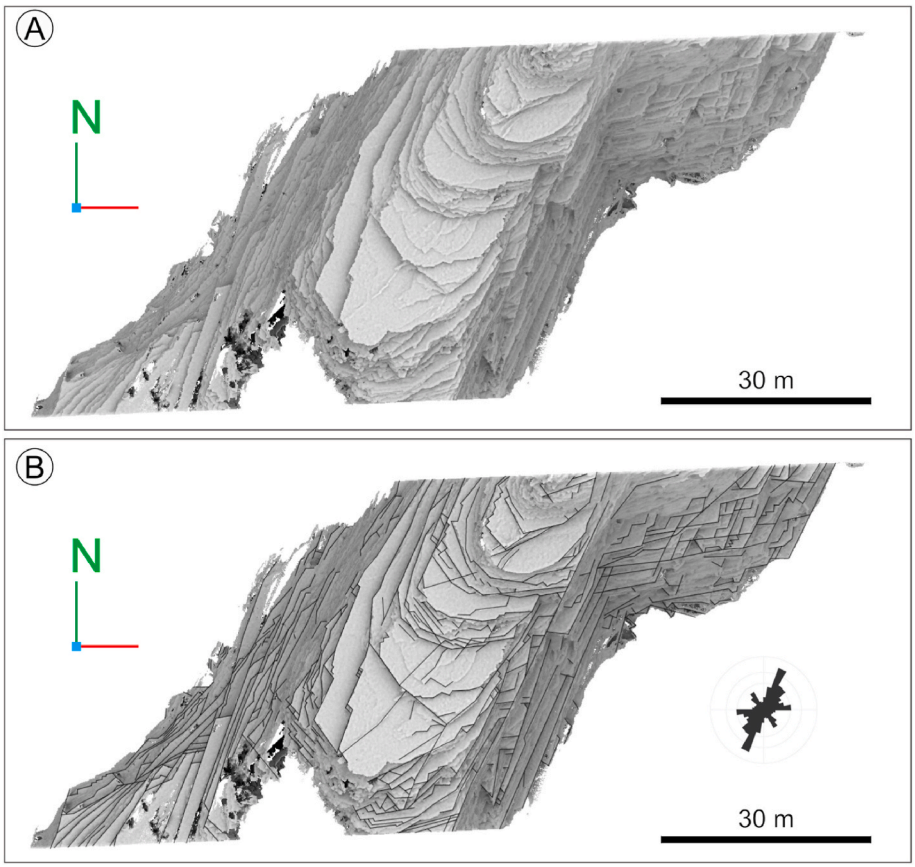

Fig. 6. Uninterpreted (A) and interpreted (B) perspective views of the Brejões cave in cross-section 8 (CS-8 in Fig. 2) created from ground-based LiDAR point cloud data.

1 and 3 (Davy, 1993; Bonnet et al., 2001). The estimated fracture trace length distributions are shown in Figs. 13 and 14, for fracture corridors and caves, respectively.

Analyses based on fracture trace length are more sensitive to sampling effects, such as truncation and censoring (Espejel et al., 2020). We then performed this analysis taking proper care to mitigate these effects (see Figs. 13 and 14) but aiming to characterize the connectivity degree of fracture networks using different approaches, in a complementary way to the other studies.

In addition, following Odling et al. (1999), we obtained the backbones of the fracture corridors. The backbones were isolated from the fracture networks by preserving the connected routes (Odling et al., 1999); that is, all "dead end" fractures were removed from the fracture networks, resulting in Fig. 15.

4.2. Statistical characterization of fractures exposed on cave surfaces

Quantitative analyses of the cave cross-sections generated from ground-based LiDAR data were performed using CloudCompare© (Compass plugin) and FracPaQ software. Because exposed surfaces might be non-flat, we gave up sampling using scan flat areas and digitized all exposed fracture traces in the images.

Structural and bedding analyses were performed using 18 cross-sections (CS-1 to CS-18) along the Brejões I main cave corridor (Fig. 2). Each cross-section has a width ranging from 50 to 100 m and provides several perspectives, at different scales, of the cave sector. Four of these CSs (CS-8, CS-10, CS-12 and CS-13) were selected to compare fracture attributes observed in the cave and in the nearest adjacent structural domains identified in Outcrop A (Figs. 7 and 8). The same statistical methodology applied to the outcrops was used in the cave cross-sections. In particular, fracture orientations were inferred from plan views of the fracture traces on the cave surfaces (Fig. 6).

4.3. Subsampling fracture corridors

This approach was used to perform topological analyses. Fracture topological analysis allows estimating the connectivity and flow properties of fracture networks (Manzocchi, 2002; Mäkel, 2007; Dimmen et al., 2017; Primaleon et al., 2020). The methodology consists of node counting inside scan areas to estimate node proportions, branch types, and connections per branch (C_B) (Sanderson and Nixon, 2015). C_B estimates are shown in Table 3 for each outcrop; each estimate represents the average value obtained from all scan areas contained in the outcrop. A circular scan area was used to avoid orientation bias in node counting (Mauldon et al., 2001; Watkins et al., 2015). We chose a diameter of 50 m for the scan areas based on two criteria: first, 98% of the fracture traces are smaller than 50 m (Fig. 10) and second, this value is a gross estimation of the lateral resolution of seismic data (Yilmaz, 2001). In addition, adequate subsampling strategies mitigate interpretation time but keep statistical reliability (Ovaskainen et al., 2022). The FracPaQ software was used to obtain a first automatic node sampling in each scan area, taking into consideration fracture intersections and isolated ends. After this, the results were manually checked.

Fracture intersections were classified as isolated (I), abutting (Y), or crossing (X) nodes. Intersections of the V type were included in the Y type. The resulting proportions of node types were expressed in ternary diagrams, as shown in Fig. 16. Branch classification followed Ortega and Marrett (2000). In this approach, branches (segments located between two nodes) were grouped into three main topological groups: I–I (isolated), I–C (partly connected), and C–C (doubly connected). To estimate branch proportions, we used the methodology proposed by Sanderson and Nixon (2015).

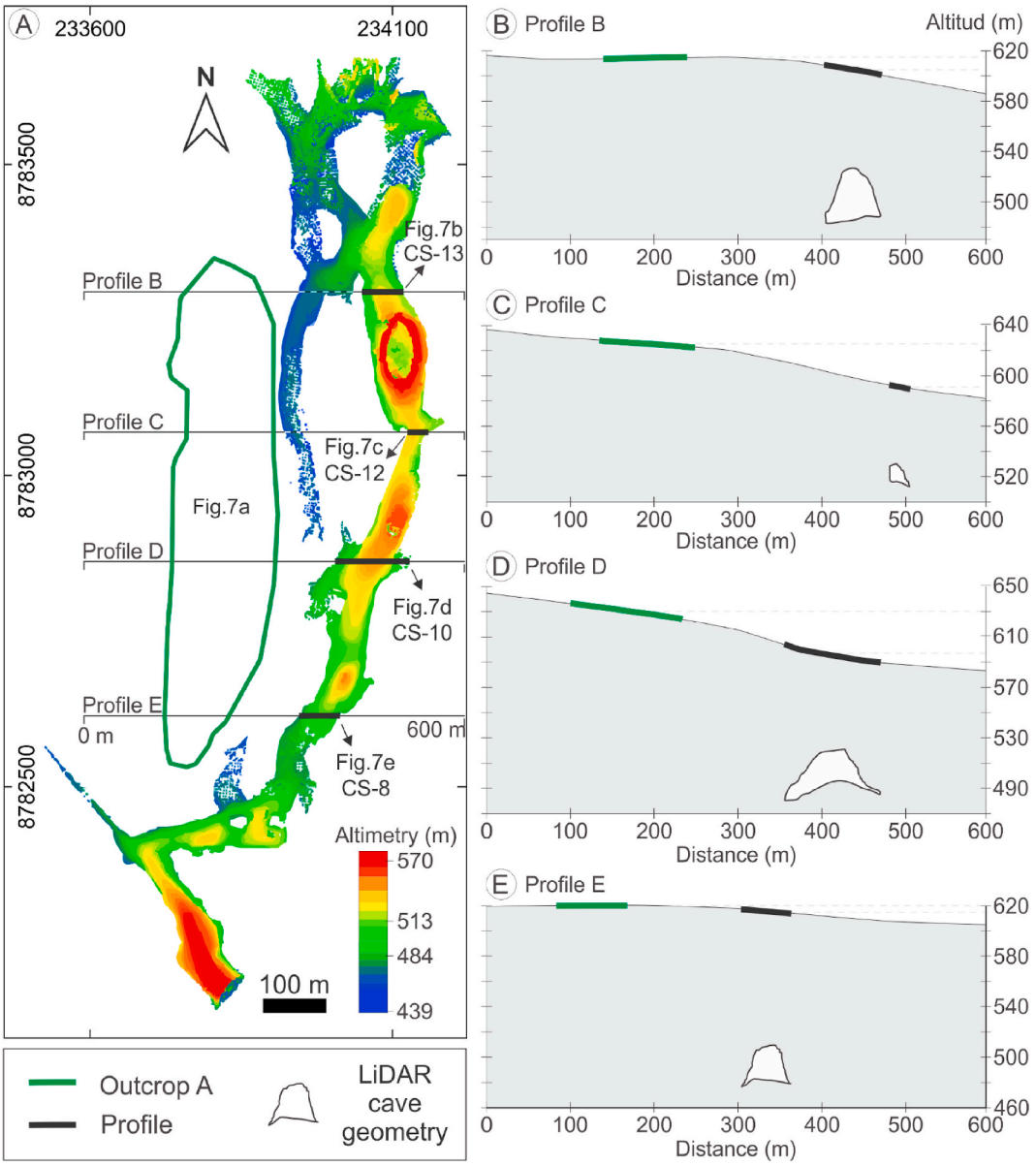

Fig. 7. Profiles B to E (thin black lines in A) crossing both the Outcrop A (green polygon) and cave sectors of the Brejões I System (shown as altimetry). The associated vertical cross-sections of the profiles are shown in (B) to (E). In (A–E), thick black lines correspond to the projections on the surface of the cave cross-sections, while in (B–E), thick green lines represent the intercepted sector of the Outcrop A. Areas around profiles B-E were used to compare the fracture directions in adjacent sectors of the outcrop and cave, as shown in Fig. 8. The cave cross-sections CS-13, CS-12, CS-10, and CS-8 (Fig. 2) correspond to the structural domains SD-I, SD-II, SD-III and SD-IV of Outcrop A shown in Fig. 8, respectively. (For interpretation of the references to colour in this figure legend, the reader is referred to the Web version of this article.)

On Outcrop A, the circular scan areas were located on sites associated with the structural domains A-I, A-II, A-IIIa, A-IIIb, and A-IV (Fig. 11). Due to the large area of the A-III domain, the topological analysis was divided into two parts (A-IIIa and A-IIIb) to allow for greater detail and better distribution of the sampling scan areas. On the other hand, in outcrops B and C (Fig. 12), the scan areas were positioned in sectors B–I to B-III and C–I to C-III, respectively, in a direction approximately perpendicular to the fold axis coinciding with the Jacaré River (see the regional structural interpretation in Section 5.2). The results of the topological analyses are shown in Fig. 16.

5. Results

5.1. General features of the study area

The UAV imagery revealed three large outcrops where karstified fracture corridors are well exposed. Each one has hundreds of meters of karst pavements (Fig. 4), which resulted from the denudation of the overlying materials that exposed the carbonate rocks to the Earth's surface. They represent fragmented remains of a much larger karst surface that was truncated by the incision by the Jacaré River. Due to the limited amount of impurities in the limestone, pedogenic processes were inhibited, and any residual soil was washed into joints, leaving a denuded flat surface.

The degree of karstification in the pavement is directly related to the length of time of exposure to meteoric dissolution, with the more

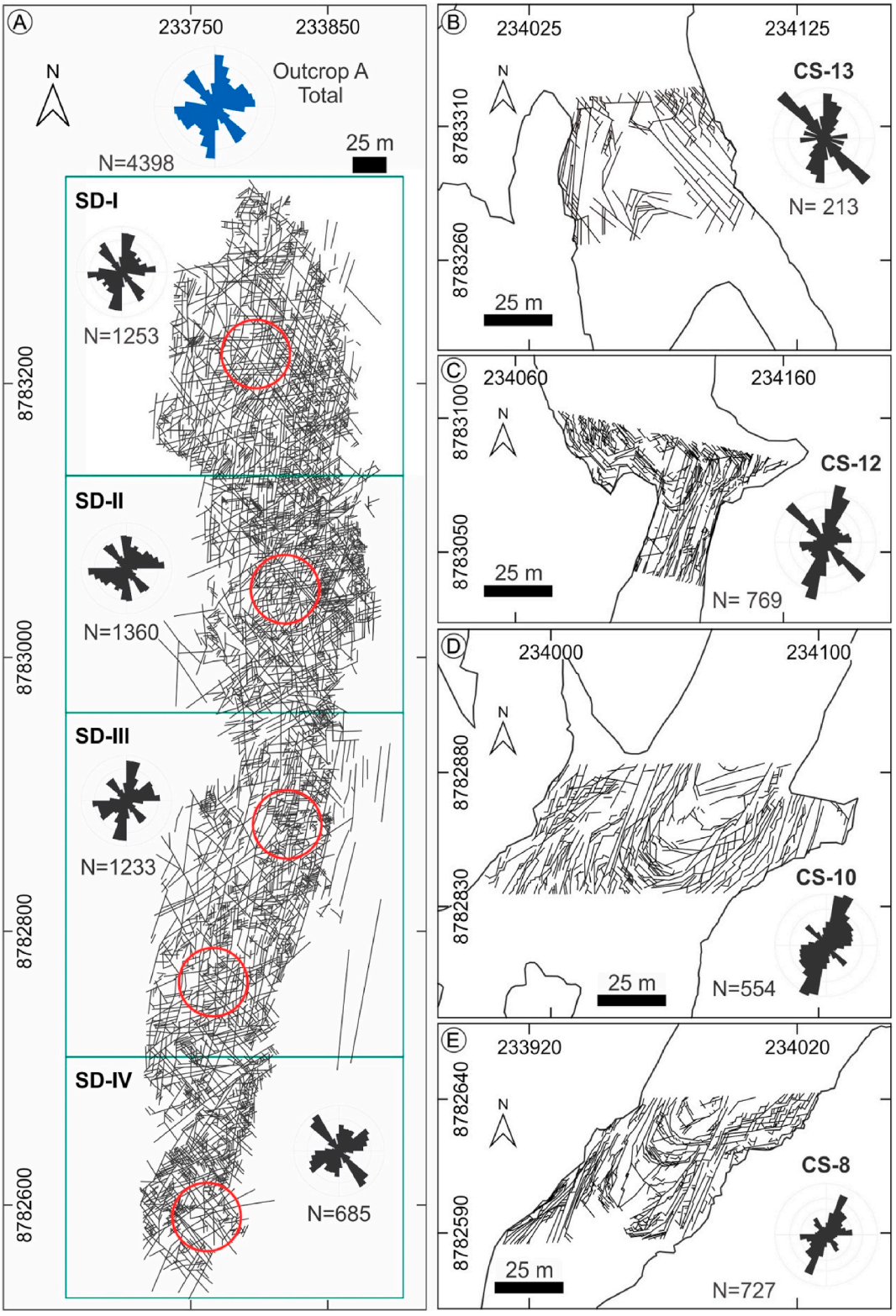

Fig. 8. Interpreted fracture traces for the adjacent sectors of Outcrop A (in A) and cave (in B-E). The interpreted structural domains SD-I, SD-II, SD-III, and SD-IV of the outcrop (in A) correspond to the cave cross-sections CS-13, CS-12, CS-10, and CS-8 (in B-E), respectively. Precise horizontal and vertical positioning of the outcrop domains and cave cross-sections are shown in Fig. 7. In Outcrop A, 4398 fractures were identified, resulting in the blue rose diagram shown in (A), while the four rose diagrams in black (also shown in A) correspond to the fracture directions in the four structural domains of the outcrop. On the other hand, in B-E, fracture directions were interpreted in the cave from ground-based LiDAR data, using interpreted views as exemplified in Fig. 6b. Note that the fracture directions are similar in adjacent sectors of the outcrop and cave. Persistence values P_{21} and P_{20} of this outcrop are shown in Fig. 11. In (A), red circles represent the five circular scan areas, A-I, A-II, A-III, A-IIIb, and A-IV, which were used to perform topological analyses (Fig. 16). (For interpretation of the references to colour in this figure legend, the reader is referred to the Web version of this article.)

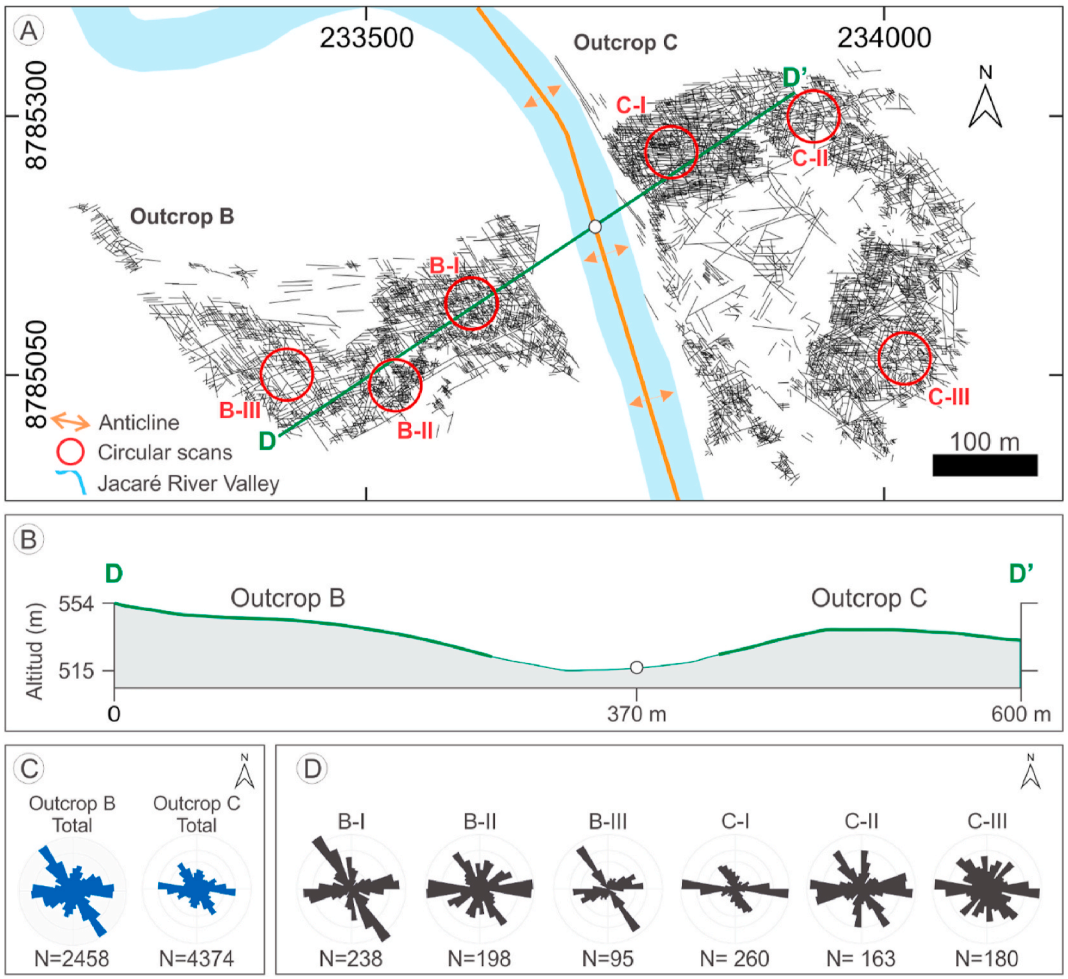

Fig. 9. Interpreted fracture traces in outcrops B and C (in A). In B, the profile D-D' (green line in A) highlights the positions of the outcrops in relation to the river valley, which corresponds to the axis of an anticline (Fig. 5); outcrops B and C correspond to the west and east fold limbs of the anticline, respectively. The resulting rose diagrams for the estimated fracture directions are shown in (C), for the whole outcrops, and in (D), for sampled sectors of the outcrops (red circles). Measures of persistence P_{21} and P_{20} are shown in Fig. 12. Red circles represent the circular scan areas used to perform topological analyses (Fig. 16). (For interpretation of the references to colour in this figure legend, the reader is referred to the Web version of this article.)

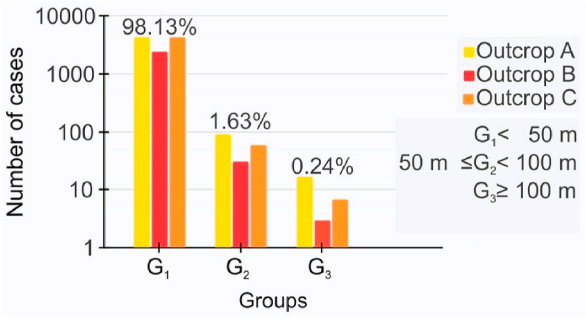

Fig. 10. Histogram of the fracture trace lengths in the three outcrops. Note that all outcrops show a predominance of fracture lengths smaller than 50 m, a value that might be taken as a gross estimate of the lateral resolution length of seismic data. The proportion of subseismic fractures is higher than 98% in all outcrops.

favorable larger fractures showing a higher degree of dissolution. This is in agreement with the results of Lopes et al. (2022), where it is evidenced that fracture enlargement due to dissolution in highly karstified outcrops is strongly influenced by fracture connectivity and little related to fracture length. All outcrops exhibit open subvertical fractures that were enlarged by karstification. The outcrops have different topographic gradients: Outcrop A is marked by subhorizontal layers from east to west, while outcrops B and C have slopes toward the NNW.

5.2. Regional structural framework

The influence of the E-W tectonics in the study area generated gentle antiforms and sinforms with N–S-oriented axes (Fig. 1). In particular, we interpret that the study area is characterized by an anticline whose axis coincides with the Jacaré River valley, as highlighted in Fig. 5. In addition, there are subvertical fracture networks composed of at least four different sets of directions (rose diagrams in Figs. 8a and 9c-d): 1) a N–S-striking set parallel to the referred anticline axis; 2) a NNE-SSW-striking set; 3) a NW-SE-striking set that we interpret as a conjugated set with the NNE-SSW-striking set; and 4) an E-W-striking set, approximately perpendicular to the anticline axis. We verified by careful inspection that there are no preferential relationships of crosscutting and abutting at the fracture terminations, a result that strongly suggests that fracture generation was coeval. In addition, the identified directions of the four fracture sets are consistent with the fracture directions generated around a folding axis (Price, 1966). These results and inferences support our interpretation that all fracture sets were generated during the anticline formation (Fig. 5).

Integrating the anticline and fracture networks results, we interpret that the study area compose the classic example of a fracture corridor

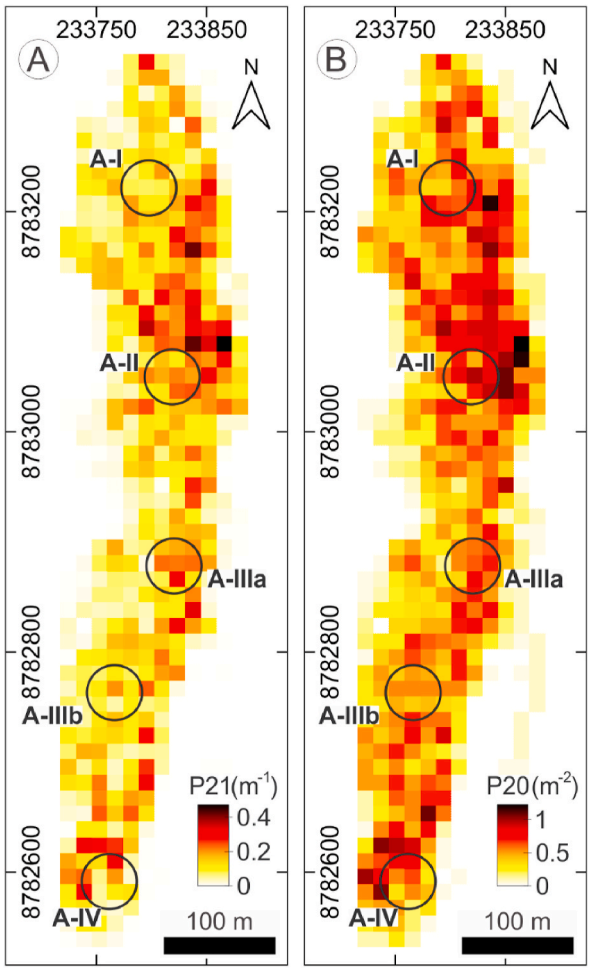

Fig. 11. Persistences P_{21} (in A) and P_{20} (in B) in Outcrop A. Note that P_{21} and P_{20} values increase from west to east. Black circles represent the five circular scan areas, named A-I, A-II, A-III, A-IIIb, and A-IV, used to perform topological analyses (Fig. 16).

installed near the hinge area of a fold (Ogata et al., 2014). On the fold axis, the N–S and NW-SE sets of fractures are dominant and contributed to the collapse of the hinge, creating a valley where the riverbed is located.

The Brejões cave system occurs farther west from the river. It is located on the left limb of the antiform. We interpret that the cave is controlled by the same four fracture sets seen in the fracture corridors. Two facts corroborate our interpretation: 1st) fracture directions in fracture corridors and caves show similar statistics (compare the rose diagrams in Figs. 8) and 2nd) fracture trace lengths in fracture corridors and caves follow similar power laws (compare Figs. 13 and 14 and estimated exponents α in Table 1). We propose that the cave was created by karstification and collapse of a former fracture corridor that developed in the limestone bedding on the limb of the fold.

Surface topography also shows imprints from the underground cave processes. For example, a dry canyon runs east from the cave passages (Fig. 3a and b), representing former hydrologically active caves of an earlier phase of Brejões I, now collapsed. These collapsed karstic valleys show abrupt limestone scarps and are surrounded by large, fractured pavements (Fig. 4), presenting a gentle dip towards the west (Boersma et al., 2019). The large carbonate outcrops expose fracture corridors (Fig. 4) with subvertical fractures generally enlarged by dissolution. Isolated truncated dolines might be aligned with existing passages, evidencing that they result from the partial collapse of conduits (Fig. 3e).

The spatial distribution of the outcrops reveals that outcrops A and B are located on the west fold limb, while Outcrop C is located on the east fold limb (Fig. 5a). All outcrops are pavement-like and are heavily fractured, showing the same four fracture sets. However, the dominance of a fracture set might vary inside the same outcrop, resulting in slightly different structural domains, as we proposed for Outcrop A (Fig. 8).

5.3. Characterization of fracture trace length and directions

We digitized a total of 11,230 fractures in the three outcrops: 4398 in Outcrop A (Figs. 8a), 2 and 458 in B, and 4374 in C (Fig. 9a). All outcrops contain fracture sets in which 98% of the fracture lengths are less than 50 m long (Fig. 10). The fracture distribution in Outcrop A is heterogeneous. As already stated, we identified at least four structural domains in this outcrop (Fig. 8a) The SD-I domain represents the northern part of this outcrop, consisting of a densely fractured and karstified part (Fig. 4a). In this area, we observed relevant contributions of all fracture sets. On the other hand, SD-II domain exhibits a higher frequency of the NNE-SSW set, while in the SD-III domain, which is the largest one, the N–S set is more evident, and the NNE-SSW set has a smaller contribution. Finally, the SD-IV domain exhibits the predominance of the NW-SE set, having a smaller contribution than the N–S set. Comparatively, outcrops B and C are more uniform (Fig. 9c–d), having an overall predominance of the NW-SE and E-W sets. As already stated, we did not perform partitions of outcrops B and C in structural domains.

We stress that the quantitative analyses of the fracture networks in the caves (Fig. 8b–e) showed the same fracture sets as observed in Outcrop A, and that they also have fracture trace lengths from centimeters to decameters Fig. 14). The geometry of the caves revealed changes in their lineament orientations. The cross-sections in the cave sectors closer to the intersections, such as CS-12, have a wide distribution of structural orientations and a higher frequency of fractures. In the subsurface, the NW-SE set is more evident in cross-sections CS-13, while the NNE-SSW fracture set is dominant in cross-sections CS-8 and CS-10, and CS-12. These facts confirm again that both the cave system and outcrops are structurally related, as proposed also by Boersma et al. (2019). We measured bedding strike dip in all 18 cross-sections (Fig. 2 and Table 2). Dip and dip direction measurements (collected directly from the cross-section) indicate that the W-E-trending plunge of the fold axis has a mean value of 5° and a mean dip direction of 283°.

5.4. Persistence measurements

Outcrop A is characterized by an increase in fracture intensity (P_{21}) and density (P_{20}) from the west toward the east (Fig. 11). The highest values of persistence occur in the A-II domain, particularly for P_{21} values. Nonetheless, on the whole, Outcrop A has the highest values of both parameters. The largest persistence values appear to be related to the relative frequency increase of the NW-SE- and NNE-SSW-striking fracture sets (Figs. 8a and 11).

On the other hand, outcrops B and C have an increase in P_{21} and P_{20} values toward the Jacaré River valley (Fig. 12c). This fact corroborates our previous interpretation that this valley corresponds to a fold hinge (Fig. 5). It is impossible to estimate P_{21} and P_{20} values in the river valley due to the lack of exposure. However, both curves suggest maximum values over the anticline axis (dashed black line in Fig. 12c).

5.5. Adherence of fracture trace length distributions to a power law and backbones of the fracture networks

The high resolution of UAV images allowed us to obtain detailed statistics of the fracture trace length distribution for each outcrop, covering more than two orders of magnitude (Fig. 13). Within the identified length limits imposed by censoring and truncation effects (Bonnet et al., 2001), power laws can be fitted to the fracture length distributions of all outcrops (Fig. 13). The fitted parameters associated

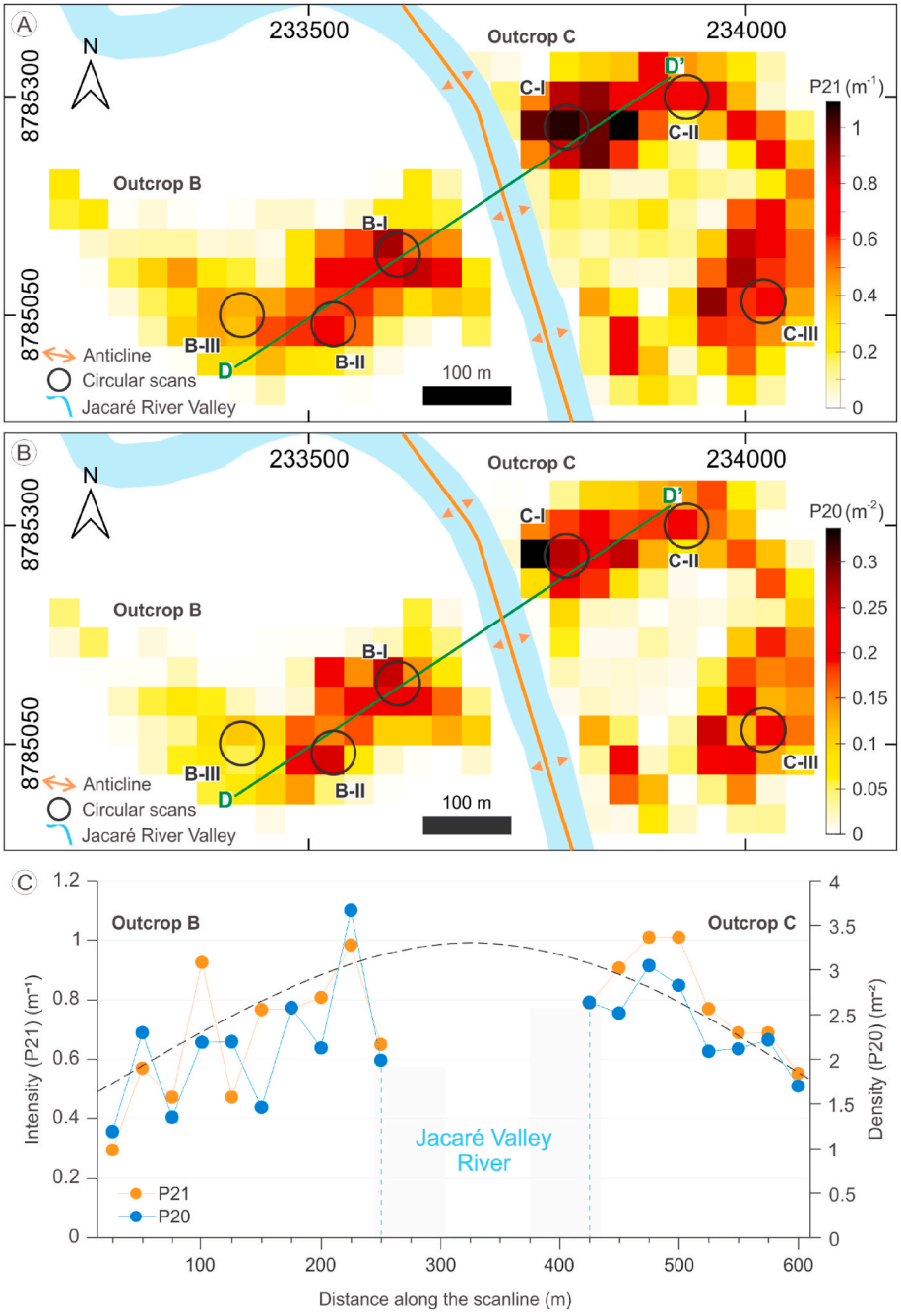

Fig. 12. Persistence values P_{21} (in A) and P_{20} (in B) in outcrops B and C. In (C), the profiles of persistence values along the line D-D' (green line both in A and B, also shown in Fig. 9a) are shown. The river valley is controlled by an anticline axis (Fig. 5), so that outcrops B and C are positioned on the west and east fold limbs of the anticline, respectively. Because of the lack of exposure, there are no measurements of P_{21} and P_{20} on the river valley, but the profile suggests maximum values for both persistences over the anticline axis (dashed black line in C). In (A) and (B), the circles represent the circular scan areas used to perform topological analyses (Fig. 16). (For interpretation of the references to colour in this figure legend, the reader is referred to the Web version of this article.)

with Eq. (1) are shown in Table 1. All fitting correlations are higher than 90% (Table 1), thus revealing good adherence to the power laws in the three datasets. In addition, we observed that all estimates of the exponent α are higher than 2.5.

According to Bour and Davy (1997), the greater the exponent α of the power law in Eq. (1), the greater the influence of small length fractures on the network connectivity. In particular, in fracture networks associated with an exponent α higher than 2.5 (all cases in this study), fractures of all measured lengths contribute to the network connectivity. In other words, the largest fractures do not dominate the network connectivity, as would be the case when the exponent α is close to 1.0 (Bour and Davy, 1997).

In addition, all fracture corridors have connectivity highly influenced by subseismic fractures (<50 m). Therefore, subseismic fractures play a key role in interconnecting fracture corridors. To corroborate these assertions, we show in Fig. 15 the backbones of the fracture networks; the backbones were obtained according to the definition of Odling et al. (1999). In accordance with the estimated values for the exponent α of the power laws (Table 1) (Bour and Davy, 1997), all backbones show clear contributions of fracture lengths of all measured sizes.

5.6. Topological analyses

We summarized the estimates of the topological parameters obtained for all outcrop sectors in Table 3. Note that C–C type of branch is strongly dominant in all outcrops (>80%, according to Table 3).

Table 3 shows also that the study area has a high proportion of $N_Y + N_X$ (>70%) and high values of C_B for all outcrops, results that are consistent with our previous interpretation that there are no preferential

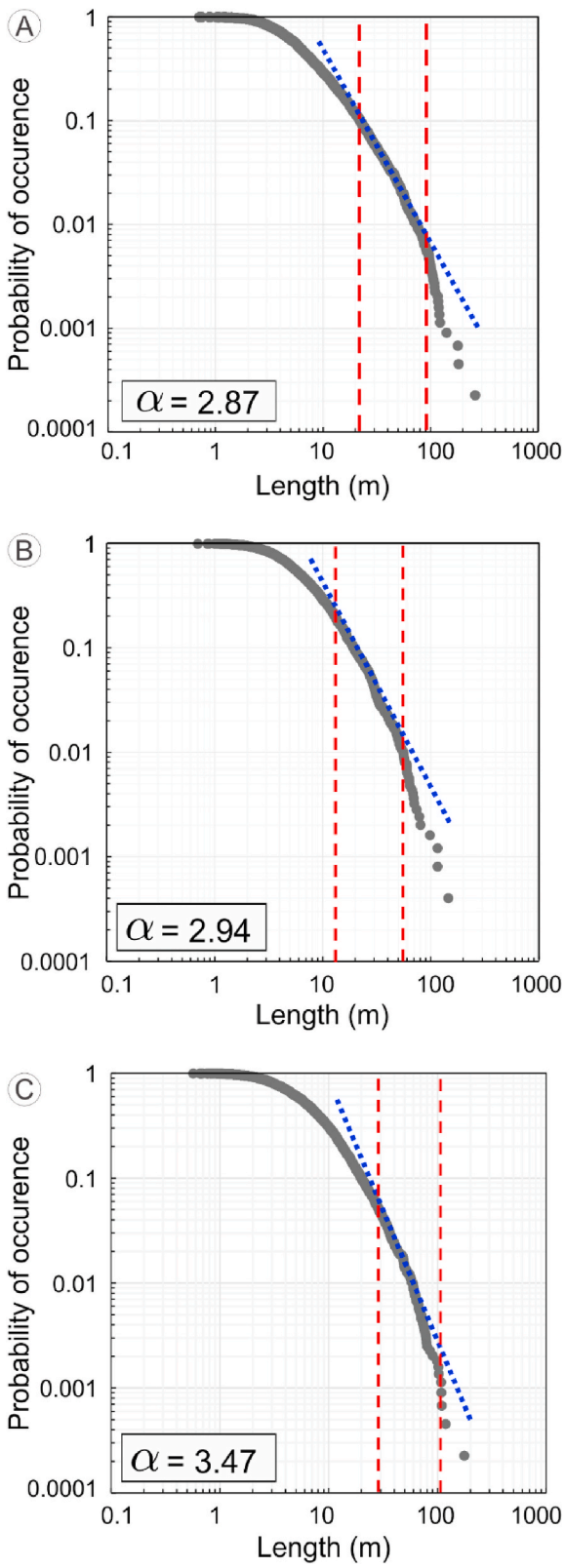

Fig. 13. Probability of occurrence of fracture trace length for outcrops A (in A), B (in B) and C (in C). The vertical lines (in dashed red) show the approximate limits of sampling validity imposed by truncation and censoring effects. The fitted power laws are shown as blue dotted lines. Table 1 exhibits the estimated values for the power-law parameters (eq. (1)). (For interpretation of the references to colour in this figure legend, the reader is referred to the Web version of this article.)

relationships of crosscutting and abutting at the fracture terminations. All outcrops show high values for the topological parameters. In particular, C_B values are close to 2.0, thus revealing that all fracture networks are highly interconnected (Sanderson and Nixon, 2018).

Differences among the three outcrops are small. Domain A-II and sector C-II appear to be the most interconnected. In the A-II case, this result also coincides with the highest values of persistence (Fig. 11). However, for Outcrop C, the C–I sector shows higher persistence values than C-II (Fig. 12a and b). We attribute this behavior to the relatively higher number of N–S fractures (Fig. 9) in promoting a higher interconnection in the C-II sector. This fact reveals the importance of joint analyses of persistence and topological parameters.

Ternary diagrams (Fig. 16a and b) show a dominance of Y and X nodes in all outcrops, as exemplified in some circular scans (Fig. 16c). In particular, a high incidence of Y nodes occurs in association with areas showing a wide distribution of fracture orientations and high values of P_{20} and P_{21}, as in the A-II, A-IIIa, and A-IV domains (Outcrop A), in addition to the B–I (Outcrop B) and C–I and C-II sectors (Outcrop C). On the other hand, a high incidence of X nodes occurs in areas where the NW-SE- and NNE-SSW-string conjugate fractures seem to be more evident, as in the A-I and A-II domains (Outcrop A), B–I and B-II (Outcrop B), and C–I sectors (Outcrop C).

The variation in node proportion (Fig. 16b) also indicates the existence of slightly distinct topological zones and thus different degrees of connectivity within the outcrops. In Outcrop A, the highest values occur in domains A-I and A-II, both densely fractured and karstified; these are also the domains that showed the highest P_{20} and P_{21}. In outcrops B and C, the B–I, C–I, and C-II sectors exhibit the highest values of the topological parameters (Table 3). These sectors correspond to areas close to the fold axis, thus corresponding to areas with high P_{20} and P_{21} (Fig. 12).

6. Discussion

6.1. Karst evolution

Karst relief in the study area resulted from a long-term geomorphical history. The present exposure of the karst pavements follows the denudation of overlying noncarbonate units in the Salitre Formation and the erosional removal of any residual pedological cover. Since no significant soil generation was possible in situ (*terra rossa*) (due to the lack of impurities in the carbonate) and mass transport was hindered (due to the lack of a gradient), denuded pavements were continuously exposed to meteoric dissolution. This was the dominant dissolution mechanism that resulted in the formation of fracture corridors with enlarged fractures.

On the other hand, the caves were created by a slightly different but related epigenic process associated with the incision of the fluvial drainage by the Jacaré River. The source area for this river is located in quartzite catchments to the south, and after they enter the carbonates, they flow underground in some sections, excavating extensive caves. The present canyon is mostly a result of the partial collapse of these caves. Collapse processes occur when the void represented by the cave passage becomes too large to support itself, generating structural instabilities. The process usually involves creating a domed ceiling in the cave that ultimately reaches the surface. This is a gradual (and ongoing) process and results in the partial collapse of the cave ceiling toward the surface. The amalgamation of collapsed areas resulted in the present canyon.

Passages at the Brejões I segment show a decreasing trend in elevation toward the west (present location of the river), suggesting a westward pattern of river migration and cave evolution (Fig. 2). Bedding plane orientation exerts an important control on the position of cave passages. Boersma et al. (2019) identified a dip toward the west in the outcrops surrounding the cave. During the fluvial-downcutting process, the river followed this trend, migrating along the bed orientation. In this scheme, the eastern passages would be older passages. This interpretation is reinforced by the presence of both truncated passages and surface

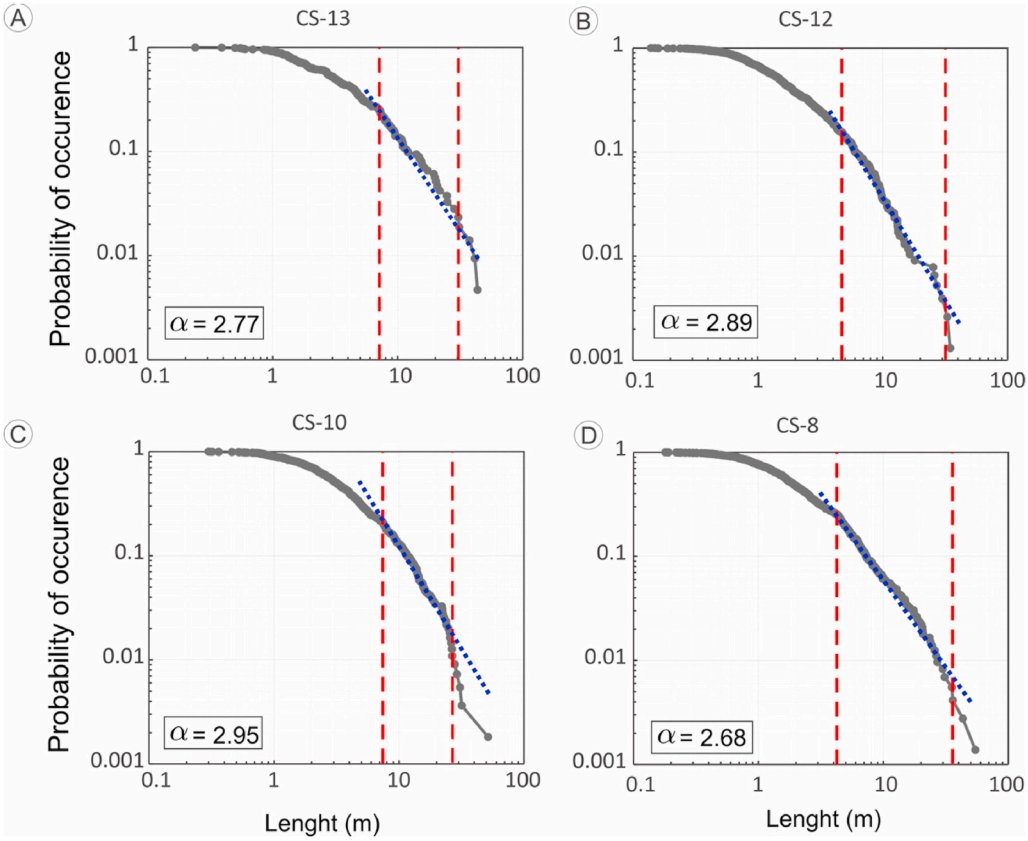

Fig. 14. Probability of occurrence of fracture trace length for the cave cross-sections CS-13 (in A), CS-12 (in B), CS-10 (in C), and CS-8 (in D). Fig. 7 shows the positions of the cave cross-sections in relation to the adjacent structural domains of Outcrop A. The vertical lines (in dashed red) show the approximate limits of sampling validity imposed by truncation and censoring effects. The fitted power laws are shown as blue dotted lines. Table 1 exhibits the estimated values for the power-law parameters (eq. (1)). (For interpretation of the references to colour in this figure legend, the reader is referred to the Web version of this article.)

canyons in the east, which probably represent ancient hydrologically active caves. Earlier hypogene processes and pyrite oxidation could have enhanced dissolution in this dominantly epigenic cave system. Although the study area is presently under a semiarid climate, there were numerous wetter intervals in the past (Wang et al., 2004), which would have considerably increased the discharge of the Jacaré River and the dissolution potential of epigenic processes in both the cave and karst pavements. Using the U-series method, Auler et al. (2004) dated tufa deposits on the valley slope just upstream from the Brejões I segment. The obtained ages ranged between 330 and 460 kyrs, showing the occurrence of significant meteoric processes at that time and that the valley attained its approximate present configuration during the mid-Pleistocene. Similar results of fracture direction statistics (Fig. 8) and trace length distributions (Figs. 13 and 14) in adjacent sectors of fracture corridors and caves (Fig. 7), indicate that karstified fracture corridors, caves and canyons developed in the study area as the final result of an advanced stage of the karst processes along the anticline axis. This process is similar to the one identified by Bagni et al. (2020) in the Jandaíra Formation (~1000 km north of the study area in the Potiguar Basin). The controlled flow of the Jacaré river along the fold hinge played a key role in the dissolution processes, especially in the formation of caves and canyons. The entire process resulted from fracture networks concentrating fluid flow percolation because of their high connectivity. In low-porosity carbonate rocks, this often results in high exposure to dissolution effects, thus creating ideal conditions for karst development.

In the three-block diagrams in Fig. 17a, we schematically summarize the evolution of this karstification scenario in near-surface carbonate rock. Due to the folding, fracture networks were created (stage I in Fig. 17a). Then, fracture epigenic enlargement began, particularly along the fold hinge, leading to the development of a structurally controlled river (stages II and III shown in Fig. 17a); in some parts, the river flows underground. The advancement of karstification process led to the formation of caves and canyons, the latter enlarged by river erosion (stage III in Fig. 17a and b). In the subsurface, karst evolution could also have caused intrabed dissolution, sometimes leading to ceiling collapse. In this situation, the formation of canyons resulted mainly from the progressive collapse of the cave ceilings that eventually reached the surface and formed dolines.

6.2. *Connectivity and percolation of the fracture networks*

Fracture corridors are often composed of fracture networks having fracture sets with different orientations (Questiaux et al., 2010; Lamarche et al., 2012; Ogata et al., 2014). Great variability in fracture orientations might allow high connectivity to the network and fracture density (Manzocchi, 2002; Sanderson and Nixon, 2018). High connectivity degrees suggest increased flow through high permeability fracture conduits (Ogata et al., 2014).

However, because fracture corridors can present very complex internal architectures, this concept has not yet been fully defined in the literature, at least from a quantitative viewpoint. Recent studies have been performed to establish spatial relationships between geometric and topological parameters related to the intrinsic architecture of fracture corridors (Espejel et al., 2020; Hermansen, 2019). Our research uses an integrated multiapproach structural analysis to show that fracture corridors formed along fold hinges have a high degree of connectivity. In particular, the predominance of terminations of types Y and X (notably Y) agrees with the results of Manzocchi (2002) and Nixon et al. (2013). As a result, fracture abutments are key contributors to the connectivity of fracture corridors, following other studies of natural fracture systems (Odling et al., 1999; Manzocchi, 2002). The major incidence of Y nodes in the areas with a wide distribution of fracture orientations and/or areas with high P_{20} and P_{21} is consistent with Manzocchi (2002). In addition, node classification indicates that fracture corridors consist of intense and connected fracture systems.

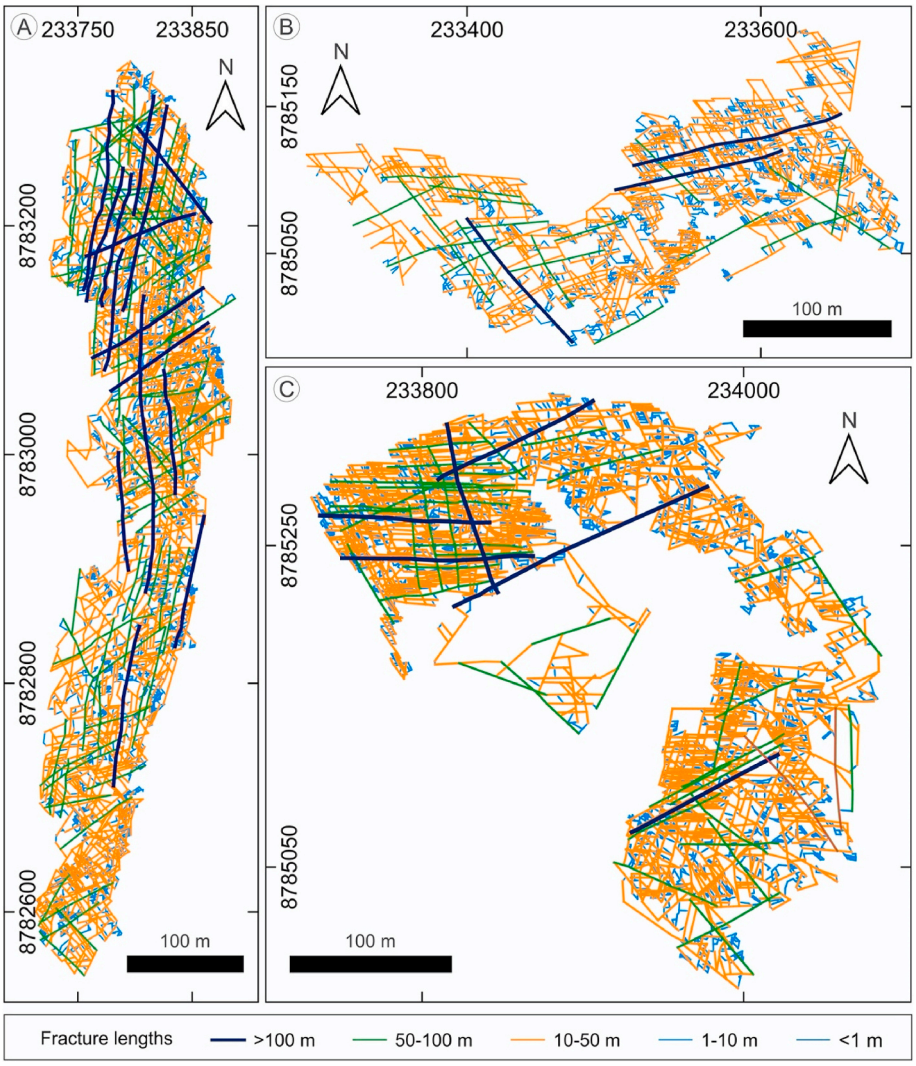

Fig. 15. Backbones of the fracture networks of the outcrops A (in A), B (in B), and C (in C). Note that the three backbones show contributions from fracture lengths of all measured sizes, a result in accordance with the fact that all estimated values for the exponent α of the power laws are close to 3.0 (Table 1) (Bour and Davy, 1997).

In turn, Bour and Davy (1997), based on computational studies of synthetic fracture networks, showed that the greater the power-law exponent Eq. (1) is, the greater the number of connections per fracture and the greater the influence of fractures of all sampled lengths on connectivity. The obtained field results corroborate this inference in the study area because all estimates of exponent α are higher than 2.5. It is important to emphasize that Bour and Davy (1997) considered only the fracture length and size of the analyzed area.

According to Sanderson and Nixon (2015), the best parameter to define fracture network connectivity is the number of connections per branch (C_B) since it can be sampled uniquely and relies less on edge effects. The C_B value is dimensionless and varies between 0 and 2; therefore, the larger the C_B, the greater the connectivity. The high C_B values estimated for the outcrops (between approximately 1.8 and 1.9, Table 3) show that all fracture networks are highly interconnected and have approximately the same average connectivity ($C_B \sim 1.9$), even for slightly different exponent values α of the power law. In addition, the C_B values indicate an increase in the connectivity degree of the cluster due to the proximity of the fold axis, following Hermansen (2019). Furthermore, we detected at least one case where topological analysis showed a high degree of connectivity even in the presence of a moderate value of persistence. These results demonstrate the importance of combined analyses of geometric, persistence and topological parameters of fracture systems.

According also to Sanderson and Nixon (2018), it is possible to obtain a reasonable indication of percolation from the average number of connections per branch for percolating systems with $C_B > 1.56$. The obtained high estimates of C_B values indicate that all fracture corridors reached the percolation threshold.

On the other hand, the power-law coefficients and backbone analyses indicate that the fluid flow routes in all fracture corridors have contributions of fracture trace lengths of all sampled sizes, particularly from subseismic lengths (<50 m). This is an important result for practical reservoir studies, which are often based on seismic images. Thus, mapping damage zones instead of mapping only seismic faults, as in Iacopini et al. (2016), might be an alternative approach to identifying fracture corridors with fracture lengths below the conventional concept of seismic resolution. Despite the limitations of fracture length analyses (Espejel et al., 2020), they added independent auxiliary information to the main conclusion derived from the topological analyses that the fracture corridors are highly interconnected.

The branch analysis provided an estimation of cluster dimensions based on C–C proportion (PCC). According to Nixon et al. (2013), cluster extension is more important than the connectivity degree since the spanning extent of the large clusters controls the percolation networks. Its extension is related to PCC; therefore, lower PCC values can be associated with isolated small local clusters, while higher PCC values represent large clusters (Sanderson and Nixon, 2018). The branch

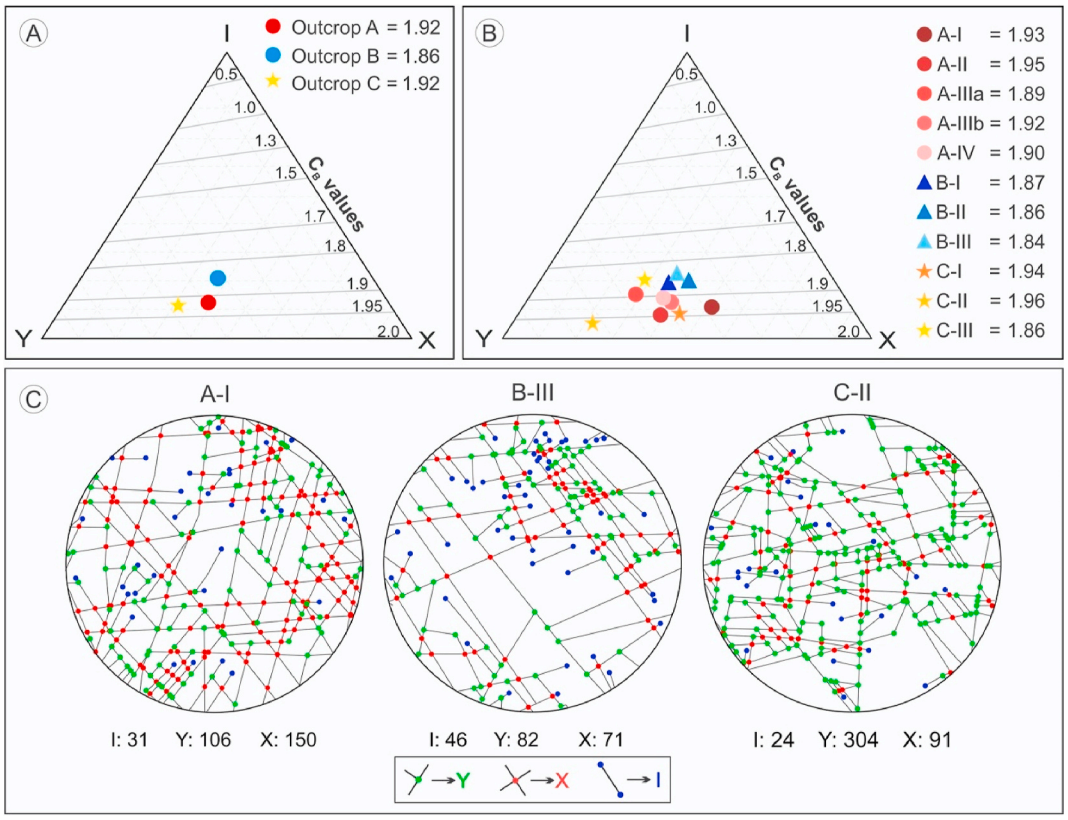

Fig. 16. Results of topological analyzes performed on eleven circular scan areas of the fracture networks in outcrops A (five areas), B (three areas), and C (three areas). Scan areas are marked in Figs. 4, 8, 9, 11 and 12 and the detailed statistical results are given in Table 3. In (A) and (B), ternary diagrams for the fracture node types are shown: in (A) taking into consideration all scan areas in a given outcrop, while in (B) for the different scan areas of each outcrop. In (C), we give examples of scan areas for the three outcrops; the chosen areas correspond to the most contrasting values identified in (B). Note that C_B values are close to 2.0 in all outcrops, thus evidencing that the fracture networks are highly connected and dominated by C–C branches (Sanderson and Nixon, 2018).

Table 1
Parameters for the fitted power laws to the probability distributions of occurrence of fracture trace lengths for fracture corridors and caves. The estimates of the power-law parameters were obtained with the software FracPaQ. The probability distribution curves are shown in Figs. 13 and 14.

Outcrop	Power-law parameters			
	Lower limit (m)	Upper limit (m)	Exponent α	Correlation coefficient
A	22.37	96.06	2.87	92.16%
B	13.18	54.38	2.94	91.20%
C	29.14	77.06	3.47	95.28%
Cave	Lower limit (m)	Upper limit (m)	Exponent α	Correlation coefficient
CS-13	7.06	30.58	2.77	99.60%
CS-12	4.94	29.90	2.89	93.28%
CS-10	7.79	26.47	2.95	94.36%
CS-8	4.28	35.80	2.68	98.40%

Table 2
Dip and dip-direction measurements collected from the Brejões ground-based LiDAR point clouds. The cross-sections (CS-1 to CS-18) are shown in Figs. 2, 7 and 8.

CS	Num. Meas.	Mean Dip (degree)	Mean Dip Dir. (degree)
1	90	005	277
2	166	005	286
3	91	005	278
4	115	005	277
5	27	005	280
6	135	005	283
7	210	004	287
8	108	004	279
9	70	004	279
10	121	005	291
11	80	005	284
12	153	006	293
13	97	005	283
14	209	005	292
15	143	005	284
16	129	005	282
17	105	005	284
18	113	004	283

Note: CS= Cross-section, Num. Meas. = Number of measurements, Mean Dip Dir. = Mean Dip Direction.

classification performed in the outcrops (Table 3) shows PCCs higher than 81%. Espejel et al. (2020) and Sanderson and Nixon (2018) also suggested that smaller fractures are more likely to form connected branches. This suggestion is consistent with the fact that approximately 98% of the mapped fracture lengths are subseismic in the study area.

Finally, all obtained results in this study conform with the general proposition (e.g., Questiaux et al., 2010) that folds might have essential control over the development of fracture corridors. In particular, the increase in persistence in the direction of the fold axis shows that fracture corridors might be curvature-controlled, developing parallel or along the hinge fold. It is important to remember the well-known fact that folds might be imaged with seismic data, thus pointing out possible locations for preferential development of fracture corridors.

6.3. *Implications for carbonate reservoirs*

Integrated studies based on geometric, topological, and persistence

Table 3
Results of topological analyses obtained from sampling circular scan areas. Topology parameters were calculated based on the methodology proposed by Sanderson and Nixon (2015). The scan areas are shown in Figs. 4, 8, 9, 11 and 12. Ternary diagrams are shown in Fig. 16.

Scan Area	Number of fractures	N_I	N_y	N_X	$N_Y + N_X$ (%)	C–C (%)	I–C (%)	I–I (%)	Total uncertainty (%)	C_B	C_B average
A-I	109	31	106	150	89.20	93.57	3.16	0.11	3.16	1.93	1.92
A-II	165	29	187	137	91.78	94.97	2.48	0.06	2.48	1.95	
A-IIIa	161	53	190	90	84.08	89.51	5.10	0.29	5.10	1.89	
A-IIIb	105	30	109	90	86.90	91.81	4.01	0.18	4.01	1.92	
A-IV	130	43	141	104	85.07	90.49	4.64	0.24	4.64	1.90	
B–I	238	108	256	197	80.75	87.44	6.07	0.42	6.07	1.87	1.86
B-II	198	112	212	224	79.56	86.84	6.35	0.46	6.35	1.86	
B-III	95	46	82	71	76.88	84.67	7.35	0.64	7.35	1.84	
C–I	260	62	316	284	90.63	94.31	2.81	0.08	2.81	1.94	1.92
C-II	163	24	304	91	94.27	96.34	1.81	0.03	1.81	1.96	
C-III	180	79	197	107	79.37	86.13	6.68	0.52	6.68	1.86	

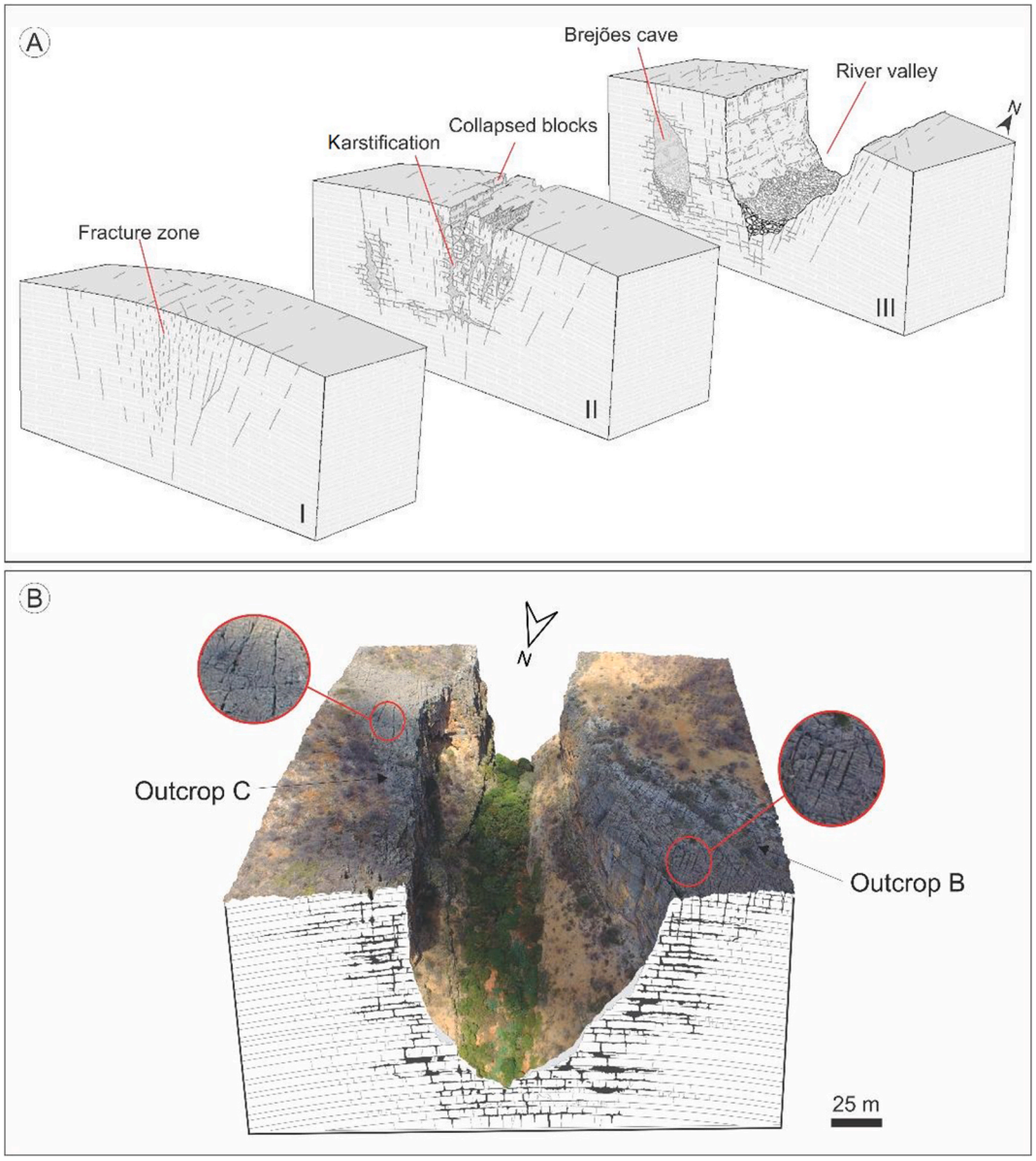

Fig. 17. Evolution model of the karstification scenario in folded carbonate rocks proposed for the Brejões System. In (A), the three block diagrams (I, II, and III) show the development of the Jacaré River valley and the karstic dissolution in the anticline hinge zone. In stage I, fracture networks are created due to folding. In stage II, fracture epigenic enlargement begins, particularly along the fold hinge, leading to the development of a structurally controlled river. In stage III, the advancement of karstification leads to the formation of caves and canyons, the latter potentialized by river erosion. In (B), a block diagram is presented, in scale, merging elements of the digital elevation model, drone photographs, and conceptual karst development (in the vertical section) to show the present configuration of the study area.

analyses of reservoir analogs can increase understanding the complex behavior of fracture networks. In rocks with low primary porosity/permeability, such as carbonates, fluid-flow properties are mainly controlled by fracture networks (Lamarche et al., 2012). Therefore, assessing how network elements are connected and distributed allows the estimation of the connectivity variability of fracture corridors. In particular, topological characterization integrated with backbone studies provides a good connectivity assessment and allows understanding how subseismic fractures might influence rock permeability. This is important because the exploratory potential of a reservoir might be underestimated as a result of insufficient sampling of its low-scale structures; that is, in the case the reservoir has fracture corridors highly influenced by subseismic fractures. Thus, integrated studies of fracture systems might help us understand some difficult reservoir management issues. For example, the high variability of well performance is often observed in fractured reservoirs, as pointed out by Questiaux et al. (2010).

Topological and backbone analyses might be carried out on different scales. In this way, it is possible to characterize the fracture network at the available scales and to attempt to upscale/downscale the obtained results for the typical scale of engineering fluid flow studies based on the fact that fracture networks might have similar parameters at different scales (e.g., Bonnet et al., 2001), as illustrated in Fig. 18. In particular, studies performed in reservoir analogs, such as the present study, might provide information to understand the data gap between the seismic and borehole scales.

Finally, our results corroborate that fracture corridors installed in folded carbonate rocks constitute preferential places for fluid flow concentration (e.g. Evans and Fischer, 2012) and karst development (e.g. Bagni et al., 2020). The high connectivity proportioned by the fracture corridors allows the concentration of preferential routes for fluid percolation, contributing to higher exposure to dissolution effects in carbonate rocks, thus creating ideal conditions for karst development.

The deformation of carbonate rocks, leading to the possible formation of folds, is a widely spread phenomenon in nature. As a result, at least two important types of carbonate reservoirs might be created, sometimes coexisting laterally in the same area. Following the classification of reservoir types I and II of Giuffrida et al. (2020), modified by La Bruna et al. (2021), they are: (a) reservoirs having large volumes of secondary porosity associated with ancient caves and canyons (type I reservoir) and (b) reservoirs composed of enlarged fracture corridors (type II reservoir). In deep condition, all spaces created by dissolution processes are infilled by other geologic materials but still strongly contribute to secondary porosity/permeability formation. Because of fracture control, the two types of reservoirs have marked anisotropies, leading to preferential routes of fluid migration and impacting all phases of reservoir exploitation.

7. Conclusions

Integrated interpretation of structural data using several approaches allowed us to conclude that fracture corridors, caves and canyons were implanted along an anticline fold hinge in the study area. The fracture corridors acted as preferential routes for fluid flow, thus creating good conditions for karst dissolution. As a result of an advanced stage of karstification involving both fracture enlargement and intrabed dissolution, karstified fracture corridors, caves and canyons were formed. In the last two cases, a river captured by the highly fractured zone of the fold hinge played an important role as an erosive agent.

The described scenario might be associated with the formation of at least two important types of carbonate reservoirs, which can coexist laterally in the same region: reservoirs composed of enlarged fracture corridors and reservoirs having large volumes of secondary porosity associated with ancient caves and canyons. In deep conditions, spaces created by dissolution processes are often infilled by other geologic materials but still strongly contribute to secondary porosity/permeability formation. Due to fracture control, the two types of oil reservoirs have marked anisotropy, leading to preferential routes of fluid migration and impacting all phases of exploitation.

Among the described results for the fracture corridors, we highlight the following. First, they reveal the high influence of subseismic fractures in connecting the fracture networks, thus indicating that this type of structure must be taken into account in reservoirs dominated by fracture corridors. In particular, large α exponents in the power laws (>2.5) indicate that relatively small-length fractures play an important role in fracture corridor connectivity. Second, in fracture corridors, node termination of types X and notably Y predominate, being the C_B values close to 2.0. Third, fracture corridors have high values of persistence P_{20} and P_{21}. Fourth, fracture networks in fracture corridors have highly interconnected backbones.

Given the importance of subseismic fractures, we suggest that deformation zone mapping is a possible alternative to identify fracture corridors with fracture lengths below conventional seismic resolution. In particular, in the case of fracture networks with lengths governed by a

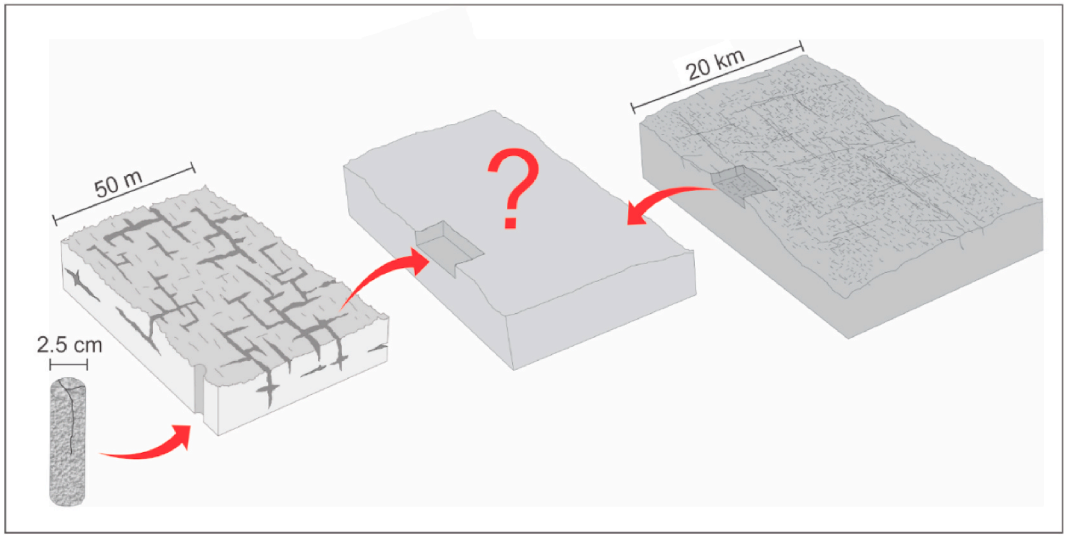

Fig. 18. Schematic block diagrams show that, in a fracture corridor, fracture directions and connectivity might be approximately the same on all scales. As a result, the information obtained by the joint interpretation of small-scale (log images, outcrop analogs) and large-scale (seismic) datasets might be used together to predict the behavior of fracture networks in the inter-well space at an intermediate scale, typical of engineering fluid-flow studies.

power law, the joint characterization of small fractures (from borehole images) and large fractures (from seismic data) might be used together to predict the behavior of fractures in the inter-well space.

Declaration of competing interest

The authors declare that they have no known competing financial interests or personal relationships that could have appeared to influence the work reported in this paper.

Acknowledgments

This research was carried out in association with the ongoing R&D project registered as ANP 20502–1, "Processos e Propriedades em Reservatórios Carbonáticos Fraturados e Carstificados – POROCARSTE 3D" (UFRN/UNB/UFRJ/UFC/Shell Brasil/ANP) – Porokarst – Processes and Properties in Fractured and Karstified Carbonate Reservoirs, sponsored by Shell Brasil under the ANP R&D levy as "Compromisso de Investimento com Pesquisa e Desenvolvimento". The Brazilian agency CNPq is thanked for the research fellowships and associated grants provided to WEM and FHRB. We also thank the "Grupo Bambuí de Pesquisas Espeleológicas" for providing the cave maps and Anderson Souza (IFPB-Picuí) for auxiliary work in surveying geodesic data. Finally, we thank JMPG Editor Tiago Alves, Roberto Espejel and an anonymous reviewer for the careful and constructive revisions of the manuscript.

References

Antonellini, M., Cilona, A., Tondi, E., Zambrano, M., Agosta, F., 2014. Fluid flow numerical experiments of faulted porous carbonates, Northwest Sicily (Italy). Mar. Petrol. Geol. 55, 186–201. https://doi.org/10.1016/j.marpetgeo.2013.12.003.

Agosta, F., Alessandroni, M., Antonellini, M., Tondi, E., Giorgioni, M., 2010. From fractures to flow: a field-based quantitative analyzes of an outcropping carbonate reservoir. Tectonophysics 490 (3–4), 197–213. https://doi.org/10.1016/j.tecto.2010.05.005.

Auler, A.S., Smart, P.L., 2003. The influence of bedrock-derived acidity in the development of surface and underground karst: evidence from the Precambrian carbonates of semi-arid northeastern Brazil. Earth Surf. Process. Landforms 28, 157–168. https://doi.org/10.1002/esp.443.

Auler, A.S., Wang, X., Edwards, R.L., Cheng, H., Cristalli, P.S., Smart, P.L., Richards, D. A., 2004. Quaternary ecological and geomorphic changes associated with rainfall events in presently semi-arid northeastern Brazil. J. Quat. Sci. 19 (7), 693–701. https://doi.org/10.1002/jqs.876.

Auler, A.S., Klimchouk, A., Bezerra, F.H.R., Cazarin, C.L., Ennes-Silva, R., Balsamo, F., 2017. Origin and evolution of Toca da Boa Vista and Toca da Barriguda cave system in North-eastern Brazil. In: Klimchouk, A., Palmer, A.N., De Waele, J., Auler, A.S., Audra, P. (Eds.), Hypogene Karst Regions and Caves of the World. Springer, pp. 827–840. https://doi.org/10.1007/978-3-319-53348-3_56.

Auler, A.S., 2019. Histórico, ocorrência e potential de cavernas no Brasil. In: Rubbioli, E., Auler, A.S., Menin, D., Brandi, R. (Eds.), Cavernas. Atlas do Brasil Subterrâneo. Editora IABS, Grupo Bambuí de Pesquisas Espeleológicas, pp. 14–51.

Bagni, F.L., Bezerra, F.H., Balsamo, F., Maia, R.P., Dall'Aglio, M., 2020. Karst dissolution along fracture corridors in an anticline hinge, Jandaíra Formation, Brazil: implications for reservoir quality. Mar. Petrol. Geol. 115, 104249. https://doi.org/10.1016/j.marpetgeo.2020.104249.

Bellian, J.A., Kerans, C., Jennette, D.C., 2005. Digital outcrop models: applications of terrestrial scanning lidar technology in stratigraphic modeling. J. Sediment. Res. 75 (2), 166–176. https://doi.org/10.2110/jsr.2005.013.

Berbert-Born, M., Karmann, I., 2000. Brejões cave, vereda romão gramacho, chapada diamantina, bahia state, Brazil. In: Schobbenhaus, C., Campos, D.A., Queiroz, E.T., Winge, M., Berbert-Born, M., Edit (Eds.), Sítios Geológicos e Paleontológicos do Brasil. Published 01/01/2000 on Internet at the address http://www.unb.br/ig/sigep/sitio016/sitio016.htm [actually. http://sigep.cprm.gov.br/sitio016/sitio016english.htm.

Bertotti, G., Audra, P., Auler, A., Bezerra, F.H., de Hoop, S., Pontes, C., Prabhakaran, R., Lima, R., 2020. The Morro Vermelho hypogenic karst system (Brazil): stratigraphy, fractures, and flow in a carbonate strike-slip fault zone with implications for carbonate reservoirs. AAPG (Am. Assoc. Pet. Geol.) Bull. 104 (10), 2029–2050. https://doi.org/10.1306/05212019150.

Bertrand, L., Géraud, Y., Le Garzic, E., Place, J., Diraison, M., Walter, B., Haffen, S., 2015. A multiscale analysis of a fracture pattern in granite: a case study of the Tamariu granite, Catalunya, Spain. J. Struct. Geol. 78, 52–66. https://doi.org/10.1016/j.jsg.2015.05.013, 721.

Bizzi, L.A., Schobbenhaus, C., Vidotti, R.M., Gonçalves, J.H., 2003. Geologia, Tectônica e Recursos Minerais do Brasil: texto, mapas e SIG. CPRM.

Boersma, Q., Prabhakaran, R., Bezerra, F.H., Bertotti, G., 2019. Linking natural fractures to karst cave development: a case study combining drone imagery, a natural cave network and numerical modelling. Petrol. Geosci. 25 (4), 454–469. https://doi.org/10.1144/petgeo2018-151.

Bonnet, E., Bour, O., Odling, N.E., Davy, P., Main, I., Cowie, P., Berkowitz, B., 2001. Scaling of fracture systems in geological media. Rev. Geophys. 39 (3), 347–383. https://doi.org/10.1029/1999RG000074.

Borges, S.V.F., Balsamo, F., Vieira, M.M., Iacumin, P., Srivastava, N.K., Storti, F., Bezerra, F.H.R., 2016. Pedogenic calcretes within fracture systems and beddings in Neoproterozoic limestones of the Irecê Basin, northeastern Brazil. Sediment. Geol. 341, 119–133. https://doi.org/10.1016/j.sedgeo.2016.05.012.

Bour, O., Davy, P., 1997. Connectivity of random fault networks following a power law fault length distribution. Water Resour. Res. 33 (7), 1567–1583. https://doi.org/10.1029/96WR00433.

Bourdon, L., Coca, S., Alessio, L., 2004. Karst identification and impact on development plan. In: SPE Asia Pacific Oil and Gas Conference and Exhibition. OnePetro. https://doi.org/10.2118/88520-MS.

Brito Neves, B.B., Fuck, R.A., Martins, M., 2014. The Brasiliano collage in South America: a review. Braz. J. Genet. 4 (3), 493–518. https://doi.org/10.5327/Z2317-4889201400030010.

Buchroithner, M.F., Gaisecker, T., 2009. Terrestrial laser scanning for the visualization of a complex dome in an extreme Alpine cave system. PFG Photogrammetrie, Fernerkundung, Geoinformation 329–339. https://doi.org/10.1127/1432-8364/2009/0025.

Buckley, S.J., Howell, J.A., Enge, H.D., Kurz, T.H., 2008. Terrestrial laser scanning in geology: data acquisition, processing and accuracy considerations. J. Geol. Soc. 165 (3), 625–638. https://doi.org/10.1144/0016-76492007-100.

Caxito, F.A.D., Uhlein, A., 2013. Arcabouço tectônico e estratigráfico da Faixa Riacho do Pontal, divisa Pernambuco-Piauí-Bahia. Revista Geonomos 21 (2).

Davy, P., 1993. On the frequency-length distribution of the San Andreas fault system. J. Geophys. Res. Solid Earth 98 (B7), 12141–12151. https://doi.org/10.1029/93JB00372.

Dershowitz, W.S., Herda, H.H., 1992. Interpretation of fracture spacing and intensity. In: Paper Presented at the the 33rd U.S. Symposium on Rock Mechanics (USRMS). Santa Fe, New Mexico.

De Waele, J., Fabbri, S., Santagata, T., Chiarini, V., Columbu, A., Pisani, L., 2018. Geomorphological and speleogenetical observations using terrestrial laser scanning and 3D photogrammetry in a gypsum cave (Emilia Romagna, N. Italy). Geomorphology 319, 47–61. https://doi.org/10.1016/j.geomorph.2018.07.012.

Dimmen, V., Rotevatn, A., Peacock, D.C., Nixon, C.W., Nærland, K., 2017. Quantifying structural controls on fluid flow: insights from carbonate-hosted fault damage zones on the Maltese Islands. J. Struct. Geol. 101, 43–57. https://doi.org/10.1016/j.jsg.2017.05.012.

Dominguez, J.M.L., 1993. As coberturas do Cráton do São Francisco: uma abordagem do ponto de vista da análise de bacias. O Cráton do São Francisco. SBG/BA-SE, SGM/BA, pp. 137–159.

Drews, T., Miernik, G., Anders, K., Höfle, B., Profe, J., Emmerich, A., Bechstädt, T., 2018. Validation of fracture data recognition in rock masses by automated plane detection in 3D point clouds. Int. J. Rock Mech. Min. Sci. 109, 19–31. https://doi.org/10.1016/j.ijrmms.2018.06.023.

Enge, H.D., Buckley, S.J., Rotevatn, A., Howell, J.A., 2007. From outcrop to reservoir simulation model: workflow and procedures. Geosphere 3 (6), 469–490. https://doi.org/10.1130/GES00099.1.

Espejel, R.L., Alves, T.M., Blenkinsop, T.G., 2020. Multi-scale fracture network characterisation on carbonate platforms. J. Struct. Geol. 140, 104160. https://doi.org/10.1016/j.jsg.2020.104160.

Evans, M.A., Fischer, M.P., 2012. On the distribution of fluids in folds: a review of controlling factors and processes. J. Struct. Geol. 44, 2–24. https://doi.org/10.1016/j.jsg.2012.08.003.

Fabuel-Perez, I., Hodgetts, D., Redfern, J., 2010. Integration of digital outcrop models (DOMs) and high resolution sedimentology e workflow and implications for geological modelling: oukaimeden Sandstone Formation, High Atlas (Morocco). Petrol. Geosci. 16 (2), 133–154. https://doi.org/10.1144/1354-079309-820.

Gallay, M., Hochmuth, Z., Kaňuk, J., Hofierka, J., 2016. Geomorphometric analyzes of cave ceiling channels mapped with 3-D terrestrial laser scanning. Hydrol. Earth Syst. Sci. 20, 1827–1849. https://doi.org/10.5194/hess-20-1827-2016.

Gillespie, P., Monsen, E., Maerten, L., Hunt, D., Thurmond, J., Tuck, D., 2011. Fractures in carbonates: from digital outcrops to mechanical models. In: Martinsen, O.J., Pulham, A.J., Haughton, P.D., Sullivan, M.D. (Eds.), SEPM Concepts in Sedimentology and Paleontology, vol. 10, pp. 137–147. https://doi.org/10.2110/sepmcsp.10.137. Outcrops revitalized: Tools, techniques and applications (pp. 3–12). Tulsa 2011.

Girardeau-Montaut, D., 2015. CloudCompare version 2.6. 1- User manual. On line at: http://www. danielgm. net/cc/doc/qCC/CloudCompare% 20v2, 6, 20.

Gholipour, A.M., Cosgrove, J.W., Ala, M., 2016. New theoretical model for predicting and modelling fractures in folded fractured reservoirs. Petrol. Geosci. 22 (3), 257–280. https://doi.org/10.1144/petgeo2013-055.

Giuffrida, A., La Bruna, V., Castelluccio, P., Panza, E., Rustichelli, A., Tondi, E., et al., 2019. Fracture simulation parameters of fractured reservoirs: analogy with outcropping carbonates of the Inner Apulian Platform, southern Italy. J. Struct. Geol. 123, 18–41. https://doi.org/10.1016/j.jsg.2019.02.007.

Giuffrida, A., Agosta, F., Rustichelli, A., Panza, E., La Bruna, V., Eriksson, M., Torrieri, S., Giorgioni, M., 2020. Fracture stratigraphy and DFN modelling of tight carbonates, the case study of the Lower Cretaceous carbonates exposed at the Monte Alpi (Basilicata, Italy). Mar. Petrol. Geol. 112 https://doi.org/10.1016/j.marpetgeo.2019.104045.

Guimaraes, J.T., Misi, A., Pedreira, A.J., Dominguez, J.M.L., 2011. The Bebedouro Formation, Una group, bahia (Brazil). Geol. Soc. Lond. Memoir. 36 (1), 503–508. https://doi.org/10.1144/M36.47.

Healy, D., Rizzo, R.E., Cornwell, D.G., Farrell, N.J., Watkins, H., Timms, N.E., et al., 2017. FracPaQ: a MATLAB™ toolbox for the quantification of fracture patterns. J. Struct. Geol. 95, 1–16. https://doi.org/10.1016/j.jsg.2016.12.003.

Hermansen, E., 2019. Mapping of Fracture Corridors in the Basement Rocks of the Øygarden Complex, Western Norway. Master's thesis. The University of Bergen.

Iacopini, D., Butler, R.W.H., Purves, S., McArdle, N., De Freslon, N., 2016. Exploring the seismic expression of fault zones in 3D seismic volumes. J. Struct. Geol. 89, 54–73. https://doi.org/10.1016/j.jsg.2016.05.005.

Jadoon, M.S.K., Jadoon, I.A.K., Bhatti, A.H., Ali, A., 2006. Fracture characterization and their impact on the field development. Pakistan J. Hydrocarbon Res. 16, 11–21.

Klimchouk, A., Auler, A.S., Bezerra, F.H.R., Cazarin, C.L., Balsamo, F., Dublyansky, Y., 2016. Hypogenic origin, geologic controls and functional organization of a giant cave system in Precambrian carbonates, Brazil. Geomorphology 253, 385–405. https://doi.org/10.1016/j.geomorph.2015.11.002.

Kuchenbecker, M., Reis, H.L.S., Fragoso, D.G.C., 2011. Caracterização estrutural e considerações sobre a evolução tectônica da Formação Salitre na porção central da Bacia de Irecê, norte do Cráton do São Francisco (BA). Geonomos. https://doi.org/10.18285/geonomos.v19i2.40.

Lagoeiro, L.E., 1990. Estudo da deformação nas sequências carbonáticas do Grupo Una na região de Irecê Bahia. Dissertação de Mestrado, Universidade Federal de Ouro Preto.

Lamarche, J., Lavenu, A.P., Gauthier, B.D., Guglielmi, Y., Jayet, O., 2012. Relationships between fracture patterns, geodynamics and mechanical stratigraphy in Carbonates (South-East Basin, France). Tectonophysics 581, 231–245.

La Bruna, V., Bezerra, F.H., Souza, V.H., Maia, R.P., Auler, A.S., Araujo, R.E., et al., 2021. High-permeability zones in folded and faulted silicified carbonate rocks–Implications for karstified carbonate reservoirs. Mar. Petrol. Geol. 128, 105046. https://doi.org/10.1016/j.marpetgeo.2021.105046.

Larsen, B., Grunnaleite, I., Gudmundsson, A., 2010. How fracture systems affect permeability development in shallow-water carbonate rocks: an example from the Gargano Peninsula, Italy. J. Struct. Geol. 32 (9), 1212–1230. https://doi.org/10.1016/j.jsg.2009.05.009.

Leão, Z.M.A.N., Dominguez, J.M.L., 1992. Plataformas Carbonáticas Precambrianas: o exemplo da Fm. Salitre - proterozoico Superior, Estado da Bahia. In: SBG, Congresso Brasileiro de Geologia, 37, São Paulo. Boletim de Resumos Expandidos, p. 451.

Lopes, J.A.G., Medeiros, W.E., La Bruna, V., de Lima, A., Bezerra, F.H.R., Schiozer, D.J., 2022. Advancements towards DFKN modelling: incorporating fracture enlargement resulting from karstic dissolution in discrete fracture networks. J. Petrol. Sci. Eng. 209, 109944. https://doi.org/10.1016/j.petrol.2021.109944.

Loucks, R.G., 2001. Modern analogs for paleocave-sediment fills and their importance in identifying paleocave reservoirs. https://doi.org/10.1306/8626CF37-173B-11D7-8645000102C1865D.

Mäkel, G.H., 2007. The modelling of fractured reservoirs: constraints and potential for fracture network geometry and hydraulics analysis. Geol. Soc. Lond. Sp. Publ. 292 (1), 375–403. https://doi.org/10.1144/SP292.21.

Manzocchi, T., 2002. The connectivity of two-dimensional networks of spatially correlated fractures. Water Resour. Res. 38 (9) https://doi.org/10.1029/2000WR000180, 1-1.

Marques Jr., A., Horota, R.K., de Souza, E.M., Lupssinskü, L., Rossa, P., Aires, A.S., et al., 2020. Virtual and digital outcrops in the petroleum industry: a systematic review. Earth Sci. Rev. 103260. https://doi.org/10.1016/j.earscirev.2020.103260.

Mauldon, M., Dunne, W.M., Rohrbaugh Jr., M.B., 2001. Circular scanlines and circular windows: new tools for characterizing the geometry of fracture traces. J. Struct. Geol. 23 (2–3), 247–258. https://doi.org/10.1016/S0191-8141(00)00094-8.

Medekenova, A., Jones, G.D., 2014. Characterization and modeling challenges associated with fracture and karst (non-Matrix) in the margin area of a carbonate reservoir (Russian). In: SPE Annual Caspian Technical Conference and Exhibition. Society of Petroleum Engineers. https://doi.org/10.2118/172275-MS.

Miranda, T.S., Santos, R.F., Barbosa, J.A., Gomes, I.F., Alencar, M.L., Correia, O.J., Falcão, T.C., Gale, J.F.W., Neumann, V.H., 2018. Quantifying aperture, spacing and fracture intensity in a carbonate reservoir analogue: crato Formation, NE Brazil. Mar. Petrol. Geol. 97, 556–567. https://doi.org/10.1016/j.marpetgeo.2018.07.019.

Misi, A., 1979. O Grupo Bambuí no Estado da Bahia. In: Geologia e Recursos Minerais do Estado da Bahia. Textos Básicos. Salvador, vol. 1. Secretaria das Minas e Energia/COM, pp. 120–154. INDA, HAV (Org.

Misi, A., 1993. A sedimentação carbonática do Proterozóico Superior no cráton do São Francisco: evolução diagenética e estratigrafia isotópica. In: II *Simpósio* Sobre O Cráton Do *São Francisco*, Resumos Expandidos, pp. 192–193. Salvador, Brazil.

Misi, A., Silva, M.G., 1996. Chapada Diamantina Oriental, Bahia. Geologia e Depósitos Minerais. Superintendência de Geologia e Recursos Minerais/Universidade Federal da Bahia, Salvador, p. 194.

Misi, A., Veizer, J., 1998. Neoproterozoic carbonate sequences of the Una Group, Irecê Basin, Brazil: chemostratigraphy, age and correlations. Precambrian Res. 89 (1–2), 87–100. https://doi.org/10.1016/S0301-9268(97)00073-9.

Misi, A., Kaufman, A.J., Azmy, K., Dardenne, M.A., Sial, A.N., de Oliveira, T.F., 2011. Neoproterozoic successions of the São Francisco craton, Brazil: the Bambuí, Una, vazante and vaza barris/miaba groups and their glaciogenic deposits. Geol. Soc. Lond. Memoir. 36 (1), 509–522. https://doi.org/10.1144/M36.48.

Nixon, C.W., Sanderson, D.J., Bull, J.M., 2013. 4. A topological analysis of 2-D fault networks and its use in assessing connectivity. ePrints Soton 75.

Odling, N.E., Gillespie, P., Bourgine, B., Castaing, C., Chiles, J.P., Christensen, N.P., et al., 1999. Variations in fracture system geometry and their implications for fluid flow in fractures hydrocarbon reservoirs. Petrol. Geosci. 5 (4), 373–384. https://doi.org/10.1144/petgeo.5.4.373.

Ogata, K., Senger, K., Braathen, A., Tveranger, J., Olaussen, S., 2014. The importance of natural fractures in a tight reservoir for potential CO2 storage: a case study of the upper Triassic–middle Jurassic Kapp Toscana Group (Spitsbergen, Arctic Norway). Geol. Soc. Lond. Sp. Publ. 374 (1), 395–415. https://doi.org/10.1144/SP374.9.

Oliveira, R.G., Medeiros, W.E., 2018. Deep crustal framework of the Borborema Province, NE Brazil, derived from gravity and magnetic data. Precambrian Res. 315, 45–65. https://doi.org/10.1016/j.precamres.2018.07.004.

Ortega, O., Marrett, R., 2000. Prediction of macrofracture properties using microfracture information, Mesaverde Group sandstones, San Juan basin, New Mexico. J. Struct. Geol. 22 (5), 571–588. https://doi.org/10.1016/S0191-8141(99)00186-8.

Ovaskainen, N., Nordbäck, N., Skyttä, P., Engström, J., 2022. A new subsampling methodology to optimize the characterization of two-dimensional bedrock fracture networks. J. Struct. Geol. 104528. https://doi.org/10.1016/j.jsg.2022.104528.

Panza, E., Agosta, F., Rustichelli, A., Zambrano, M., Tondi, E., Prosser, G., Janiseck, J.M., 2016. Fracture stratigraphy and fluid flow properties of shallow-water, tight carbonates: the case study of the Murge Plateau (southern Italy). Mar. Petrol. Geol. 73, 350–370. https://doi.org/10.1016/j.marpetgeo.2016.03.022.

Price, N.J., 1966. Fault and Joint Development in Brittle and Semi-brittle Rocks. Pergamon, Oxford.

Priest, S.D., 1993. Discontinuity Analysis for Rock Engineering. Chapman & Hall, London, United Kingdom, p. 473.

Primaleon, L.P., McCaffrey, K.J.W., Holdsworth, R.E., 2020. Fracture attribute and topology characteristics of a geothermal reservoir: southern negros, Philippines. J. Geol. Soc. 177 (5), 1092–1106. https://doi.org/10.1144/jgs2019-126.

Questiaux, J.M., Couples, G.D., Ruby, N., 2010. Fractured reservoirs with fracture corridors. Geophys. Prospect. 58 (2), 279–295. https://doi.org/10.1111/j.1365-2478.2009.00810.x.

Rubbioli, E., Auler, A.S., Menin, D., Brandi, R., 2019. Cavernas. Atlas Do Brasil Subterrâneo. Editora IABS, Grupo Bambui de Pesquisas Espeleológicas, p. 340p.

Sanderson, D.J., Nixon, C.W., 2015. The use of topology in fracture network characterization. J. Struct. Geol. 72, 55–66. https://doi.org/10.1016/j.jsg.2015.01.005.

Sanderson, D.J., Nixon, C.W., 2018. Topology, connectivity and percolation in fracture networks. J. Struct. Geol. 115, 167–177. https://doi.org/10.1016/j.jsg.2018.07.011.

Santana, A., Chemale, F., Scherer, C., Guadagnin, F., Pereira, C., Santos, J.O.S., 2021. Paleogeographic constraints on source area and depositional systems in the neoproterozoic Irecê Basin, São Francisco craton. J. S. Am. Earth Sci. 109, 103330. https://doi.org/10.1016/j.jsames.2021.103330.

Silvestre, I., Rodrigues, J.I., Figueiredo, M., Veiga-Pires, C., 2015. High-resolution digital 3D models of Algar de Penico Chamber: limitations, challenges, and potential. Int. J. Speleol. 44 (1), 25–35. https://doi.org/10.5038/1827-806X.44.1.3.

Singh, S.K., Abu-Habbiel, H., Khan, B., Akbar, M., Etchecopar, A., Montaron, B., 2008. Mapping fracture corridors in naturally fractured reservoirs: an example from Middle East carbonates. First Break 26 (5). https://doi.org/10.1016/S0191-8141(00)00094-8.

Slob, S., Hack, R., Turner, A.K., 2002. An approach to automate discontinuity measurements of rock faces using laser scanning techniques. In: ISRM International Symposium-EUROCK 2002. International Society for Rock Mechanics and Rock Engineering.

Souque, C., Knipe, R.J., Davies, R.K., Jones, P., Welch, M.J., Lorenz, J., 2019. Fracture corridors and fault reactivation: example from the chalk, isle of thanet, kent, England. J. Struct. Geol. 122, 11–26. https://doi.org/10.1016/j.jsg.2018.12.004.

Souza, S.L.D., Brito, P.C.R., Silva, R.W.S., 1993. Estratigrafia, sedimentologia e recursos minerais da Formação Salitre na Bacia de Irecê, Bahia. Salvador. Companhia Baiana de Pesquisa Mineral (CBPM), p. 36, 1993. (Série Arquivos Abertos 2).

Thiele, S.T., Jessell, M.W., Lindsay, M., Ogarko, V., Wellmann, J.F., Pakyuz-Charrier, E., 2016. The topology of geology 1: topological analysis. J. Struct. Geol. 91, 27–38. https://doi.org/10.1016/j.jsg.2016.08.009.

Trice, R., 2005. Challenges and insights in optimising oil production form middle eastern karst reservoirs. In: SPE Middle East Oil and Gas Show and Conference. Society of Petroleum Engineers. https://doi.org/10.2118/93679-MS.

Wang, X., Auler, A.S., Edwards, R.L., Cheng, H., Cristalli, P.S., Smart, P.L., Richards, D.A., 2004. Wet periods in northeastern Brazil over the past 210 kyr linked to distant climate anomalies. Nature 432, 740–743. https://doi.org/10.1038/nature03067, 2004.

Watkins, H., Bond, C.E., Healy, D., Butler, R.W., 2015. Appraisal of fracture sampling methods and a new workflow to characterise heterogeneous fracture networks at outcrop. J. Struct. Geol. 72, 67–82. https://doi.org/10.1016/j.jsg.2015.02.001.

Weismüller, C., Prabhakaran, R., Passchier, M., Urai, J.L., Bertotti, G., Reicherter, K., 2020. Mapping the fracture network in the Lilstock pavement, Bristol Channel, UK: manual versus automatic. Solid Earth 11 (5), 1773–1802. https://doi.org/10.5194/se-11-1773-2020.

Yilmaz, O., 2001. Seismic Data Analysis. Society of Exploration Geophysicists, Tulsa, USA.